Design and Techno-economic Assessment of a New Hybrid System of a Solar Dish Stirling Engine Integrated with a Horizontal Axis Wind Turbine for Microgrid Power Generation

Bashar Shboul[1,2], Ismail AL-Arfi[1], Stavros Michailos[1], Derek Ingham[1], Omar H. AL-Zoubi[2], Lin Ma[1], Kevin Hughes[1], Mohamed Pourkashanian[1]

[1]Energy 2050, Department of Mechanical Engineering, Faculty of Engineering, University of Sheffield, Sheffield S3 7RD, UK

[2]Renewable Energy Engineering Department, Faculty of Engineering, Al al-Bayt University, Mafraq, Jordan

Abstract

The increasing interest in renewable microgrids have motivated the exploration of more sustainable alternatives to traditional energy supply. In this study, a novel hybrid renewable energy-based microgrid power system is proposed, designed and techno-economically assessed. The system consists of a concentrated parabolic solar dish Stirling engine and a horizontal axis wind turbine integrated with a battery bank. The novelty of the study lies in replacing conventional hybrid systems, such as a typical photovoltaic/wind assembly, with a novel solar dish/wind turbine system that has the potential to achieve higher efficiencies and financial competitiveness. The solar dish Stirling engine serves as the primary source of electrical power generation while the horizontal axis wind turbine, in conjunction with a battery bank, supplies backup electricity when the primary source of power is unavailable. The system has been designed through advanced modelling in the MATLAB/ Simulink® environment that efficiently integrates the individual energy technologies. A technical sensitivity analysis has been performed for all the units in order to reduce the respective design limits and identify optimum operational windows. Further, the performance of the model has been tested at two locations in Jordan, and a thorough techno-economic analysis of the integrated system has been conducted. The simulation results show that at the optimal design point the efficiency of the Stirling engine is 37% with a net output power of 1500 kWe. For the horizontal axis wind turbine, a module of 100 kWe with a power coefficient of 0.2-0.24 is suitable for operation in terms of cost, power, torque and farm size. Also, two economic indicators, namely, the levelised cost of electricity and hourly cost, have been calculated. The levelised cost of electricity lies between 0.13 and 0.15 $/kWh while the hourly cost is found to be around 4 $/h. Thus, the economic evaluation revealed that the proposed system is very competitive with other integrated renewable energy technologies.

Keywords: Microgrids; Hybrid system; Horizontal axis wind turbine; Solar dish engine; Stirling engine

1. Introduction

In this section, a general overview of the factors that drive hybrid renewable energy technologies are presented as well as some of the benefits and features that the implementation of concentrated parabolic solar dish Stirling engines (CPSD-SE) can offer. Further, a summary of published works related to the development of CPSD-SE and their integration into microgrids is investigated along with the research gaps that the current study aims to fill. Finally, the main objectives of the research are discussed.

1.1 Background

Due to the damaging effects on the environment from the worldwide consumption of conventional energy resources, it has become paramount to find renewable energy-based systems to mitigate greenhouse gas emissions and, at the same time, to provide cost-effective solutions to protect against any future inflation in energy prices [1]. Nevertheless, all renewable energy technological solutions bring with them certain disadvantages. In particular, the majority are stochastic, dispersive, and in general are not easily accessible, and they come with distinct regional variabilities [2]. For these reasons, hybrid renewable energy systems (HRES) have been proposed by experts to eliminate the intermittent output of individual systems and enhance their efficiency [3].

Hybridisation by integrating various energy resources has many advantages, including the reduction of specific capital costs, an increase in the capacity of power generation, enhancement of reliability and overall efficiency as well as it provides more flexibility to the optimisation of the design [4]. The most common hybridisation configuration is combining solar and wind energies. Further, a microgrid system comprising of HRES is one of the most efficient energy alternatives that are expected to satisfy the energy demands of remote regions. In general terms, microgrids can be defined as clusters of electrical energy generators, energy storage and controllable loads in combination with a central control system to monitor their operation and distribute generation sources that operate in both grid-connected and off-grid modes [5]. Moreover, the small-scale decentralised distributed generation systems are now becoming a promising alternative to the typical large-scale centralised power plants [6] at remote locations [7]. Most of the hybrid microgrids generations are accomplished by integrating photovoltaic (PV) arrays with wind turbines (WT)

[8]. Nassar et al. [9] applied techno-economic optimisation of a stand-alone hybrid PV/wind power system to electrify an urban community in Libya. Based on the cost analysis, the levelised cost of electricity (LCOE) was estimated to be 0.236 $/kWh. An alternative solution to PVs is the concentrated solar power (CSP) plants, especially dish concentrators that have higher electrical efficiency than PV plants of similar size. For example, the CPSD-SE has the highest conversion efficiency, ranging from 16% to 31%, among the CSP based technologies [10]. In comparison, the most efficient commercial solar PV has an efficiency that ranges between 13 and 20% [11]. Further, a CSP plant can harness direct normal solar irradiation (DNI) that is usually more than 2000 kWh/m^2, (>5 kWh/m^2/day [12]). Moreover, CSP plants typically possess lower environmental impacts than PV plants over their entire life cycle due to the less intensive assembling and decommissioning phases [13]. In summary, the CPSD-SE system has the potential to become an attractive solution due to its great potential in enhancing the microgrids performance as well as providing an eco-friendly energy conversion system. As a result, the scope of the present research is to assess a hybrid system based on the CPSD-SE technology.

The Middle East and North Africa (MENA) countries have abundant solar and wind energy resources available and Jordan is considered to be a good typical example of such a region. Therefore, the MENA region has a great potential to integrate the most advanced CSP technologies [14]. Further, the German Aerospace Center (DLR) stated [15] that by 2025 the CSP technologies would play a leading role in the Mediterranean region that would promote a broad mix of renewable technologies. Consequently, CSP will have a considerable portion of the RES generation in the MENA countries. More specifically, Jordan has a relatively abundant annual DNI of 2700 kWh/m2, and in addition, the average number of sunny days per year is nearly 300 with 3311 hours per year. For the wind speed, Jordan has a high potential of annual average wind speed at some locations with higher than 7 m/s and with highs of 10 m/s [16]. Thus, Jordan has been selected as a suitable region to test the performance of the proposed microgrid but it should be also highlighted that the same design and modelling approaches can be implemented in many other locations in the world.

1.2 Literature review

It is apparent that there is a lack of studies that deal with the integration of HRES with solar thermal power cycles based on external combustion engines such as SE. Also, an

implementation of a hybrid CPSD-SE/HWT system in decentralised microgrids for power generation has not been previously studied in the literature.

A small number of techno-economic studies exist in the literature regarding CPSD-SE systems. One of these studies was a theoretical analysis conducted by Wu et al. [17] by means of a parametric study to determine the overall performance of the CPSD-SE system. The performance evaluation results revealed that 18.54 kWe of electrical power could be generated with an overall thermal–electric efficiency of 20.6%. Another study, focusing on the techno-economic feasibility of the CPSD-SE system under varying conditions, was conducted by Poullikkas et al. [18] in a number of Mediterranean regions, but principally in Cyprus. The researchers conducted a parametric cost-benefit analysis using a special algorithm as a simulation tool. Further, a techno-economic viability of a 100 MWe CSP plant consisting of 4000 of 25 kWe CPSD-SE units in Algeria has been investigated by Abbas et al. [19]. The System Advisor Model (SAM) software, developed by The National Renewable Energy Laboratory (NREL), was implemented for a techno-economic assessment to estimate the monthly and yearly energy production.

Ruelas et al. [20] conducted a theoretical examination to assess the technical feasibility of a Scheffler-type CPSD-SE using a new mathematical model. Ruelas's model involves three parameters namely the geometric, optical and thermal models of the receptor. Reddy and Veershetty [21] conducted a techno-economic feasibility analysis of the autonomous power plant for a 5 MWe CPSD-SE collector at over 58 locations in India. To reach high values for the average annual power generation of 12.68 GWh, the parametric analysis included such factors as the land area required and energy yield. Based on the economic performance, the minimum LCOE for CPSD-SE power plant was 0.197 $/kWh, with a payback period of 10.63 years. Bakos and Antoniades [22] conducted a techno-economic study of a large scale CPSD-SE power plant in Greece, utilising the TRNSYS software. This simulation tool was utilised to simulate the performance as well as to assess the feasibility of the proposed installation of the solar power plant consisting of 1000 units CPSD-SE, each with a nominal power of 10 kWe. The results showed that the annual energy production of the proposed power plant could reach 11.19 GWh, and achieving a 16 years pay-back period.

Al-Dafaie et al. [23] proposed a mathematical model of a CPSD-SE system based on the average hourly data across six different days measured from the Energy Center of the Jordan University of Science and Technology, Jordan. A techno-economic performance analysis has

been carried out to investigate the potential of utilising the rejected heat from the cold chamber in the solar Stirling engine (SE) for potable water production in the distillation process. Further, a mathematical model was utilised by Mendoza et al. [24] in order to identify the maximum geometric configuration parameters of the solar tracking system control that is designed to improve the solar system efficiency of a CSPD-SE system. The performance results indicated that a maximum thermal efficiency of 25% could be reached at a solar radiation of 1000 W/m^2 and diameter at 10.5 m. Bataineh and Taamneh [25] simulated a stand-alone CPSD-SE with a battery bank using the SAM software tool. The results revealed an overall net system efficiency of approximately 21% and a lowest LCOE of about 0.102 $/kWh. Zayed et al. [26] established and thermodynamically modelled a new commercial Solar Dish/Stirling system with a rated power of 25 kWe; the levelized energy cost of the system was found to be ~0.256 $/kWh. Buscemi et al. [27] investigated and optimised the energy performance of a 32kWe CPSD-SE system. Shaikh et al. [28] investigated a performance model of a 25 kWe stand-alone CPSDS-SE system. The results indicate that the system could produce annual electricity of 38.6 MWh with a net efficiency of 23.39% and LCOE of 0.13 $/kWh.

In the future, it is expected that more CPSD-SE applications will be commissioned due to the technology's suitability for hybridisation [29]. Nevertheless, only a few studies have addressed the hybridisation of a CPSD-SE with other power generation systems in microgrids. Guo et al. [30] established a new hybrid steam/air biomass gasification integrated with CPSD-SE for combined cooling, heating and power (CCHP) system in China. The authors conclude that this novel hybrid system obtains an energy efficiency of 51.34%. Mastropasqua et al. [31] have studied the integration of CPSD-SE with a solid oxide electrolysis cell to produce electricity, thermal energy and hydrogen. It has been shown that the system can be operated at a nominal solar-to-hydrogen efficiency of above 30% and producing 30 kWe and 150 kg/d of hydrogen.

For the hybridisation of CPSD-SE/HWT, Shariatpanah et al. [32] introduced a new grid-connected hybrid power system coupled with a typical CPSD-SE and a WT. The results of the simulation indicated that a new hybrid on-grid CPSD-SE/WT could provide an acceptable performance. Rahman et al. [33] investigated the automatic generation control of a hybrid CPSD-SE and a WT by assessing the generation rate and speed governor dead band constraint. Kadri and Hadj Abdallah [34] conducted a technical performance analysis of a hybrid CPSD-

SE/WT connected to the electricity distribution grid in a coastal area located in Tunisia. It is clear from the literature that the power range (10-50 kWe) of the CPSD-SE system is suitable and decentralised for the small and micro scales (residential and small commercial applications) of power generation.

Based on the literature review, it is clear that there exists a lack in the literature of studies dealing with the modelling and the techno-economic design of the CPSD-SE/HWT integrated solution. The present study aims at filling this knowledge gap and adopts a comprehensive approach in assessing the feasibility of the proposed novel system. The new assembly configuration has a number of important features: (a) the generator position, usually placed in the receiver of each dish, helps to mitigate heat losses and provides flexible modular operation (typical sizes varying between 5 and 50 kWe) and hence it is ideal for distributed generation of various scales, (b) the CSPD-SE collectors do not require large cooling systems (e.g. cooling towers) and therefore electricity can be supplied in regions that water supply is restrained, (c) CSPD-SE has a low noise engine and simple structural design with fewer moving parts than other CSP systems, (d) CSPD-SE systems achieve high concentration ratios (more than 3000) and high efficiencies of about 30%. Due to these features, the CPSD-SE/HWT has the potential to be economically attractive and this is thoroughly investigated within this study.

1.3 Objectives

An innovative and user-friendly modelling approach has been applied that facilitates the interaction among the different assembly components, i.e. CPSD-SE, HWT and battery bank and this fosters the optimisation of the microgrid. The CPSD-SE is the prime mover in the absence of solar irradiation, the HWT and the battery bank operate to provide the required electricity. The design procedure and the assessment performance of the microgrid have been exemplified in two regions within Jordan, namely Madaba and Mafraq. The main objectives of this work are as follows:

- Design of the proposed system through advanced modelling to integrate the decentralised microgrid system. Models have been developed in the MATLAB/Simulink® environment and have been used to evaluate the size and design of the system and to ensure that the electrical demand of the end-user is met.

- Construction of a sensitivity assessment on the developed system to investigate the effects of various design parameters on the system performance.
- Implementation and in-depth testing of the system in two regions in Jordan.
- A detailed techno-economic assessment of the proposed hybrid CPSD-SE/HWT system with energy storage for microgrid applications.

2. Methods

In this section, the methods, assumptions, and mathematical modelling are presented. It is also important to identify and analyse the geographical location of the case study. Accordingly, the meteorological characteristics of the examined locations are presented.

A robust modelling tool using the MATLAB/Simulink® software that uses actual weather data obtained from SolargisTM has been developed. The model platform contains the following subsystems that are fully and well-integrated with each other: CPSD-SE, HWT, battery bank, meteorological model, cost unit and control unit. Most importantly, all mathematical model equations are solved simultaneously, unlike other software that solves each component separately. The proposed model is constructed based on a design approach, which is used to calculate and measure the system size and cost. The inlet system parameters, indicated in Tables 2, 3, and 4, are assigned by the user and then the entire design data (size and cost) is calculated. Effective control strategies have been implemented to manage the system operation and distribute the power load between the sub-systems. Moreover, the economic model gives a high resolution for the cost through calculating the hourly cost and LCOE. The current model provides the foundation of the microgrid design and, as future research, it could be optimised through multi-objective optimisation.

2.1 System description

The proposed system is suitable for power generation on a residential scale (100-1500 kWe) and Figure 1 shows a schematic diagram of the proposed hybrid CPSD-SE/HWT stand-alone microgrid power system for residential application. The system is mainly composed of three subsystems which are CPSD-SE, HWT and battery banks. The CPSD-SE is utilised as the primary source of electricity generation, whilst the HWT and battery bank will supply backup electricity when the primary source of power is unavailable. This strategy ensures the

continuity of power generation. The CPSD-SE system is designed with an assembly of parabolic dish collectors and a power conversion unit that includes a thermal receiver, a SE and an alternator. Furthermore, this work aims to study the design of the system over one year of operation in two locations in Jordan, i.e. Mafraq and Madaba. The assigned power and efficiencies are used to calculate the size and the cost. It is assumed the grid charges the batteries bank. However, in a future work, the performance model will be integrated in which the efficiency and the generated power of the existing system will be measured depending on the predesign analysis. The batteries bank in this case will be charged by the CPSD-SE and HWT. The main feature that distinguishes the CPSD-SE from other types of solar technologies, i.e. PV and CSP, is its ability to transform the solar radiation directly into electrical and thermal power. In principle, the CPSD-SE mirrors reflect the incident sunlight to a focal point on a thermal receiver (i.e. the hot chamber of the SE), thereby converting the concentrated radiation at the receiver into thermal energy to produce heat at a high temperature and it then transfers the absorbed heat into the SE working fluid. It is anticipated by the CPSD-SE to generate 25-30 kWe of nominal power per module. In the case of absence of sunlight, the required power is supplied by the HWT and when a low wind speed occurs from the batteries. A three-blade design is adopted in this work, and the HWT is expected to generate 50-100 kWe of rated power. The control room unit is responsible for the load variation between the system units.

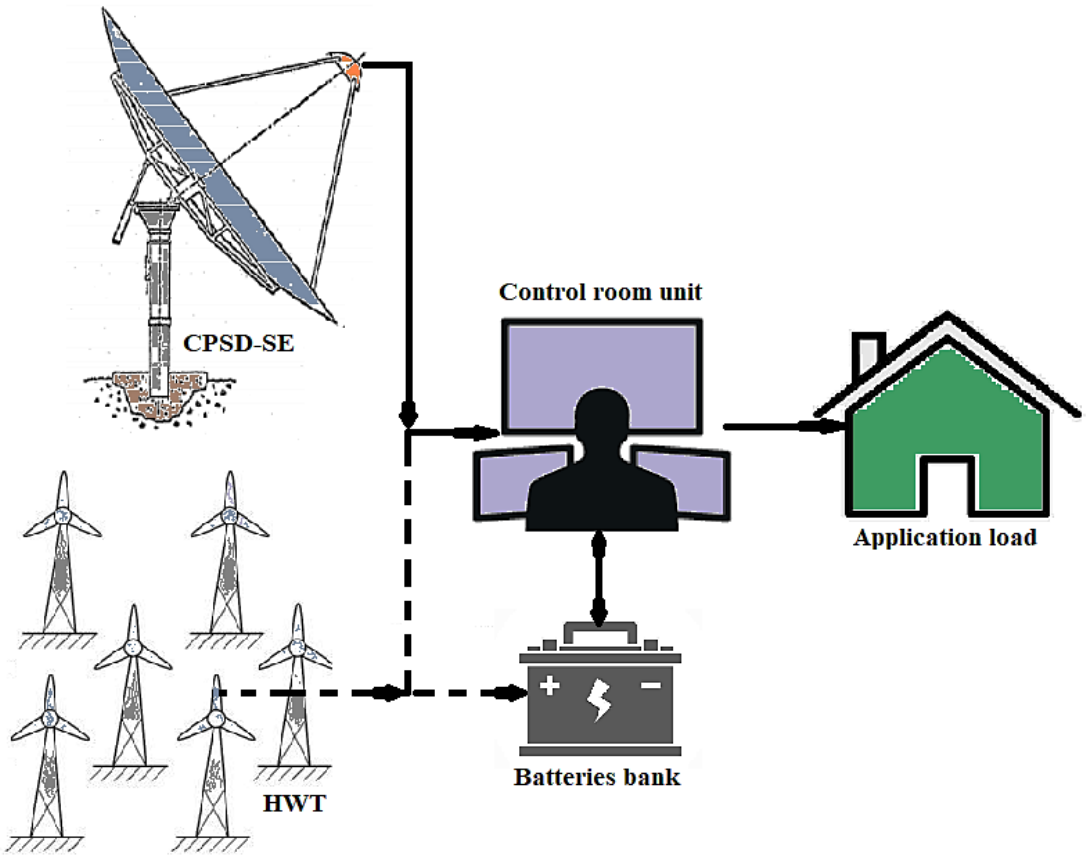

Figure 1. Schematic diagram of the proposed new hybrid CPSD-SE/HWT

2.2 Meteorological data and site selection

Jordan has substantial solar energy resources that are likely to be able to meet most of its electricity demand. In addition, Jordan is located in the earth-sun belt region with a relatively high range of daily solar irradiance, ranging from 3.8 to 8 kWh/m^2 [35] and this implies a potential of 2700 kWh/m^2 DNI per annum [36]. Furthermore, the average sunshine duration is approximately 300 days a year [37], with an average daily sunshine of 9.07 hours or 3311 hours per annum. Thus, due to the abundant availability of solar radiation, the extensive desert region (unsuitable for agriculture) within the country, the low rainfall and the overcast skies make the selection of Jordan as being one of the most suitable locations for implementing solar energy technologies. In addition, Jordan is windy, with an annual average wind speed in some parts of the country being more than 7.5 m/s (with highs of 11.5 m/s) [38]. Currently, wind energy is mainly used for water pumping at a low to moderate rate while for power generation its usage is limited. Figure 2 shows the potential of solar and wind energies over Jordan [39], which can be considered as being substantial. Further, in order to

measure the solar radiation and the wind speed over Jordan, a large set of weather data inputs (>100,000 points (1999-2019)) have been obtained from Solargis^{TM} [39].

In particular, two locations, Mafraq and Madaba, are selected to examine the techno-economic competitiveness of a 1500 kWe CPSD-SE/HWT system. Mafraq is located in the north of Jordan (32.34^0 N, 36.21^0 E) and it is semi-desert: hot, dry weather in summer and cold weather in winter. Madaba is located in the central region of Jordan (31.72^0 N, 35.79^0 E) and has a Mediterranean climate: hot summers, rainy winters. Table 1 provides the meteorological parameters of the two selected regions [40].

Table 1. The meteorological information of the proposed locations.

Region	Air temperature (°C)			GHI (kWh/m^2)			DNI (kWh/m^2)			Wind speed@100 m (m/s)		
	Mean	Max	Min	Mean	Max	Min	Mean	Max	Min	Mean	Max	Min
Mafraq	18.6	20.4	16.8	5.8	6.01	5.75	6.9	7.29	6.54	6.0	7.5	4.6
Madaba	21.8	24.8	18.8	5.7	5.93	5.44	6.1	6.94	5.31	5.3	6.0	4.6

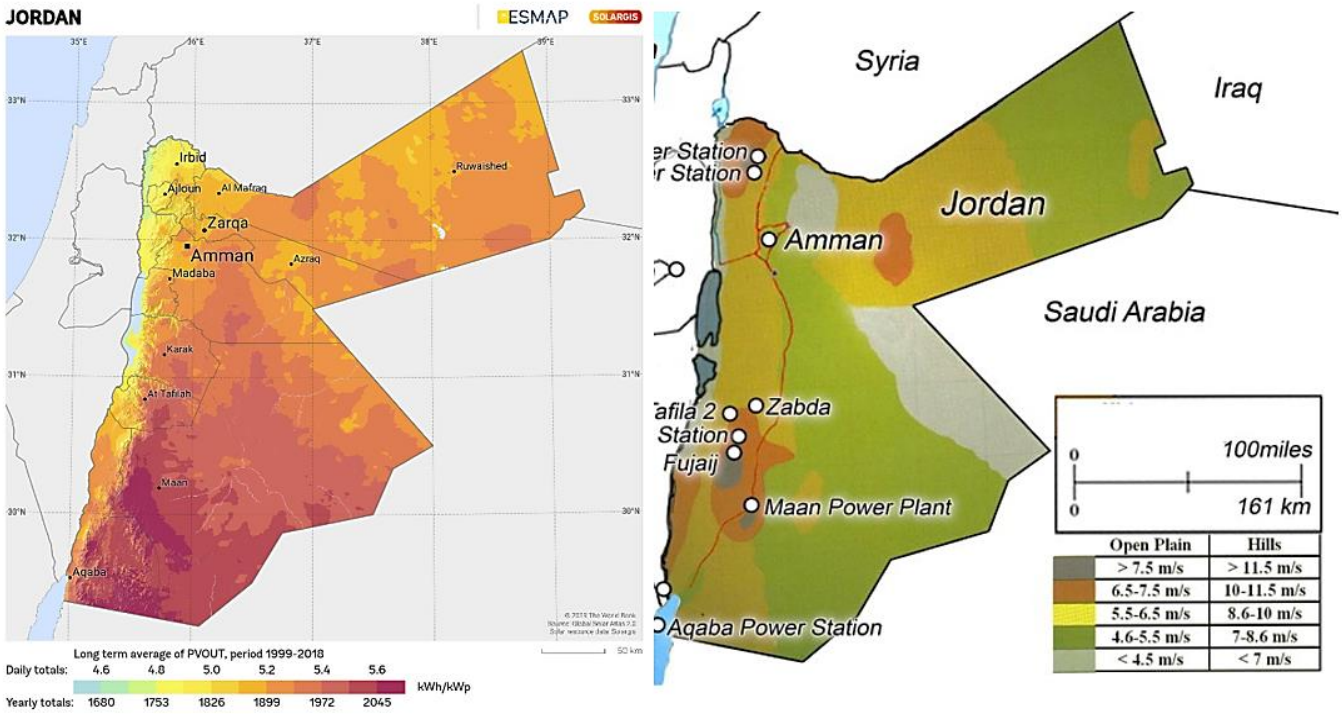

Figure 2. Solar and wind energies potential in Jordan.

2.3 Mathematical modelling

The mathematical models describing each technology of the proposed integrated energy system are based on the fundamental energy balance equations and the governing

thermodynamic equations have been implemented and solved in the MATLAB/Simulink® environment. The model consists of several Simulink blocks, which are stored as icons in an intensive visual Simulink library to construct a complete thermodynamic model. This visual library allows the user to drag-and-drop icons to build distinct configurations. Accordingly, this feature facilitates the user to execute further calculations, such as sizing and economic calculations. Figure 3 shows the model browser of the proposed system. The developed thermodynamic model possesses the following assumptions:

- All the processes and components are assumed to be in steady-state.
- The changes in potential and kinetic energy are not considered to be significant.
- All working fluid properties are acquired at their average temperature.
- The pressure drops and heat losses system components are not considered in order to minimise the complexity of the developed numerical model.
- The SE's hot chamber temperature is set to be the same as the receiver's temperature.
- The power load is assigned as an input parameter in order to accomplish the design and sizing of the system units. It is fluctuated to simulate the real-time operation. It is assumed that the power range does not exceed 1500 kWe (suitable for small communities).

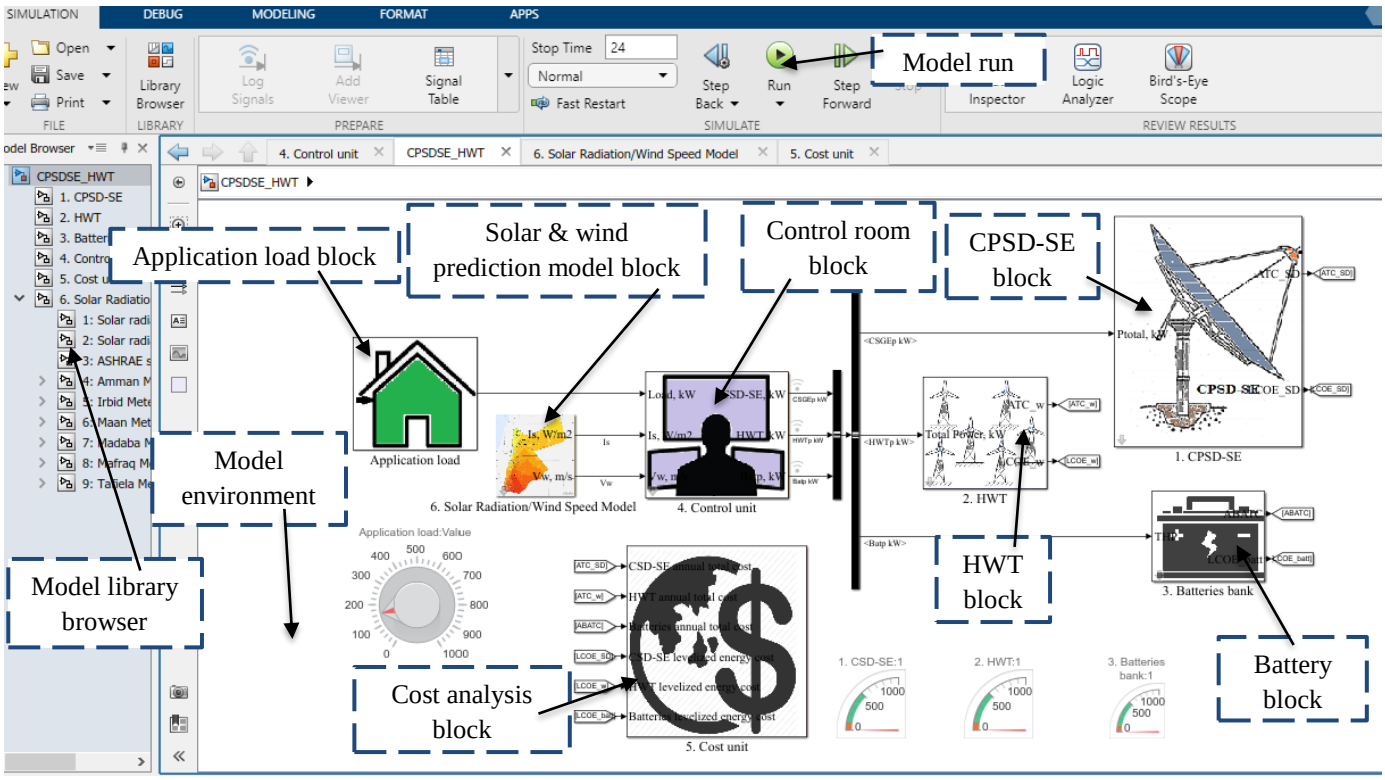

Figure 3. The developed model browser in the MATLAB/Simulink® toolbox environment.

2.3.1 The battery bank mathematical model

Starting with the modelling of the battery bank, the technical specifications are taken from the manufacturer's manual and the inputs of the design parameters for the battery are summarised in Table 2. Applying these parameters, the battery storage model is simulated and designed using MATLAB/Simulink®. The simulation results that have been estimated include: battery storage capacity, E_b, battery amp-hours, *AH*, load current, I_l, and number of batteries, *NOB.* The equations (1)-(6) are representing the battery calculation model.

Table 2: The input parameters to the battery storage system.

Data	Symbol	Unit	Value
Total Power of the battery	$P_{tot,b}$	*kW*	100 - 1500
Operating hours	*OH*	*hour*	*12*
No. of cloudy days factor	*NOC*	*day*	*2*
Battery efficiency	η_b	*%*	*75*
Battery depth of discharge	*DOD*	*%*	*80*
Load voltage	V_l	*V*	*200*
Battery voltage	V_b	*V*	*80*
Battery current	I_b	*A*	*10*

The battery bank capacity (*Wh*) is calculated as follows [41]:

$$E_b = \frac{P_{tot,b} \times OH \times NOC}{\eta_b \times DOD} \quad (1)$$

The required amp-hours of the batteries (*Ah*) [42]:

$$AH = \frac{E_b}{V_l} \quad (2)$$

Load current (A):

$$I_l = \frac{P_{tot,b}}{V_l} \quad (3)$$

Number of batteries can be calculated as follows [43]:

$$X_b = \frac{V_l}{V_b} \quad (4), Y_b = \frac{I_l}{I_b} \quad (5), NOB = X_b \times Y_b \quad (6)$$

2.3.2 The horizontal axis wind turbine mathematical model

In a similar manner, the HWT model has been developed using the MATLAB/Simulink® toolbox and the input data employed in the simulation process are listed in Table 3. The

generated power load on the turbine unit is assigned in order to calculate the remaining design parameters such as hub height, H_h, air mass flow rate, M_{air}, rotor swept area, A_r, axial force, F_x, rotor torque, T_{or}, power coefficient, C_p, required wind power, P_w, No. of HWT, N_{wt}, spacing in wind direction, X_s, spacing cross the wind direction, Y_s, and farm total area, A_{tot}.

Table 3: The input parameters to the HWT system.

Data	Symbol	Unit	Value
Air pressure	P_{air}	*bar*	1.01
Air temperature	T_{air}	^oC	15-25
HWT module power	P_m	*kWe*	10-500
Total power of HWT	$P_{tot,t}$	*kWe*	500-8000
Average wind speed	V_{wr}	*m/s*	1.5
Rated rotor speed	*RPMr*	*rpm*	28.5
Rotor diameter	D_r	*m*	47
Load factor	*LF*	-	0.9
Generator efficiency	η_g	-	0.97

The proposed HWT model is assessed through the use of the equations (7)-(19). The main parameters that affect the module power are the air density, power coefficient, and turbine swept area. Hence, the hub height (m) is given as follows [44]:

$$H_h = 1.25 \times D_r \tag{7}$$

Air mass flow rate (*kg/s*) is obtained as follows:

$$M_{air} = \rho_{air} \times A_r \times V_{wr} \tag{8}$$

where the air density (kg/m^3) is calculated as follows:

$$\rho_{air} = \frac{P_{air} \times 100}{0.287 \times (T_{air} + 273.15)} \tag{9}$$

Rotor swept area (m^2) is given as:

$$A_r = \pi \times \left(\frac{D_r}{2}\right)^2 \tag{10}$$

Axial force (*kN*) is given by [42]:

$$F_x = \frac{4}{9000} \times \rho_{air} \times A_r \times \left({V_{wr}}^2\right) \tag{11}$$

Rotor torque (*N.m*) is determined as [45]:

$$T_{or} = \frac{(1000 \times P_m)}{\omega} \tag{12}$$

where the rotor speed (*rev/s*) is calculated as:

$$\omega = \frac{(2 \times \pi \times RPM_r)}{60} \quad (13)$$

The required wind power is estimated as follows [46]:

$$P_w = \frac{\left(\frac{1}{2} \times \rho_{air} \times A_r \times \left(Vw_r{}^3\right) \times LF \times \eta_g\right)}{1000} \quad (14)$$

The power coefficient is given as follows [47] :

$$C_P = \frac{P_m}{P_w} \quad (15)$$

The number of wind turbines required can be calculated as follows:

$$N_{wt} = \frac{P_{tot,t}}{P_m} \quad (16)$$

Optimum spacing in a row is given by [44]:

$$X_s = 12 \times D_r \quad (17)$$

Optimum spacing in the cross wind direction is given by [44]:

$$Y_s = 3 \times D_r \quad (18)$$

The total land area (Km^2) is obtained through the following equation:

$$A_{tot,t} = 2 \times X_s \times Y_s \times N_{wt} \quad (19)$$

2.3.3 The concentrated parabolic solar dish Stirling engine mathematical model

In this section, the mathematical equations of the CPSD-SE are presented. Typically, these numerical equations include measures of the CPSD-SE components, namely, SE, dish concentrator, cavity receiver, and alternator as expressed in equations (20)-(45) [48]. The first sub-model is the opto-geometric model that evaluates the geometrical parameters and the configurations of the receiver and concentrator system by equations (20)-(25). The second model is the thermal analysis model that utilises the thermodynamic balance of the investigated system to calculate its performance using equations (26)-(45). For the thermal energy balance model, a rate of sunlight incidence on the dish mirrors is used for the electricity generation; it should be noted that the generated thermal power is not considered in this investigation. Consequently, the energy balance of the developed thermodynamic model has been achieved by considering the following assumptions:

- The receiver heat losses by conduction are neglected since they are insignificant.
- The optical heat loss is neglected.
- The heat rejected from the SE is neglected.

- The generator, concentrator, and receiver efficiencies are given.

Table 4 presents the inputs of the design parameters for the CPSD-SE and the simulation results of the proposed CPSD-SE are the dish concentration ratio, CR_{dish}, dish area, A_c, receiver area, A_r, total plant area, A_{tot}, number of solar dishes, N_{dishes}, focal length, f, Stirling engine efficiency, η_{SE}, total efficiency, η_o, engine compression ratio, CR_{SE}, engine pressure ratio, R_{PSE}, piston volume, V_p and piston stroke.

Table 4: The input parameters of the CPSD-SE system.

Data	Symbol	Unit	Value
Operating conditions			
Operating hours	*OH*	*hr*	10
Solar radiation	I_s	W/m^2	1000
Ambient temperature	T_{amb}	^oC	15-35
Design limits			
Total plant power	P_{tot}	*kWe*	25-1000
Stirling engine parameters			
Working fluid type	Helium (H_e), Air, Hydrogen (H_2), Nitrogen (N2), Carbon dioxide (CO_2)		
SE power	P_{SE}	*kWe*	15-30
SE speed	$\vec{V}_{SE}$	*rpm*	1800
SE piston diameter	D_p	*cm*	5.5
Number of SE cylinders	NOC_{SE}	-	4
High cycle temperature	T_h	^oC	400-800
Lower cycle temperature	T_l	^oC	15-35
Initial cycle pressure	P_{atm}	*bar*	1.023
Dish concentrator parameters			
Rim angle	ψ_r	*degree*	37
Receiver efficiency	η_r	*%*	70-80
Generator efficiency	η_{gen}	*%*	95
Concentrator efficiency	η_c	*%*	97

For the geometric model, the dish concentrator diameter is calculated as follows:

$$D_c = \left(\frac{A_c}{\frac{\pi}{4}}\right)^{\frac{1}{2}} \tag{20}$$

The rim angle ratio, f/D_c is given by [48]:

$$RAR = 1.003 \times e^{-\left(\frac{\psi_r - 11.28}{13.86}\right)^2} + 2.186 \times e^{-\left(\frac{\psi_r + 100.2}{127.6}\right)^2} \quad (21)$$

The focal length can be written as follows [49]:

$$\mathfrak{f} = RAR \times D_c \quad \text{or} \quad \mathfrak{f} = \frac{D_c}{4 \times tan\left(\frac{\psi_r}{2}\right)} \quad (22)$$

The dish height (m) is calculated from the following equation [50]:

$$H_{dish} = \frac{{D_c}^2}{16 \times \mathfrak{f}} \quad (23)$$

The receiver diameter:

$$D_r = \left(\frac{A_r}{\frac{\pi}{4}}\right)^{\frac{1}{2}} \quad (24)$$

The maximum height of the focal point is obtained as follows [24]:

$$H_r = \mathfrak{f} - d_{\mathfrak{f}} \quad (25)$$

For thermal analysis model, the SE efficiency is calculated as follows [51]:

$$\eta_{SE} = 0.5 \times \left[1 - \left(\frac{T_1 + 273}{T_h + 273}\right)\right] \quad (26)$$

The concentrator efficiency is obtained as follows [10]:

$$\eta_c = \rho_m \times F_{sh} \times \Gamma \quad (27)$$

Where: ρ_m is the mirror reflectance, F_{sh} is the U-shading factor, and Γ is the intercept factor.

The optical efficiency is obtained by the assigning receiver efficiency [52]:

$$\eta_{opt} = \eta_c \times \eta_r \quad (28)$$

The total efficiency of the module can be written as [26]:

$$\eta_o = \eta_{SE} \times \eta_{gen} \times \eta_{opt} \quad (29)$$

The dish concentration ratio, A_d/A_r is given as [48]:

$$CR_{dish} = \frac{\sigma}{0.9 \times \alpha_{rec} \times I_s \times \Psi}, \sigma = 5.669 \times 10^{-8} \quad (30)$$

$$\Psi = \left(\frac{T_{amb} + 273}{T_h + 273}\right) \times \left(\frac{1}{5 \times (T_h + 273)^4 - (T_{amb} + 273)^4 + 4 \times (T_h + 273)^3}\right) \quad (31)$$

The compression ratio of the SE, based on the efficiency, is determined as follows [53]:

$$CR_{SE} = e^{\left(\frac{1 \times C_v}{R \times C_s}\right)} \quad (32)$$

$$C_s = \frac{\left(\frac{1-\frac{1}{\xi}}{\eta_{SE}}\right)-1}{1-\left(\frac{1}{\xi}\right)} \quad (33)$$

$$\xi = \frac{T_h + 273}{T_l + 273} \quad (34)$$

The high-pressure (*kPa*) can be obtained as follows [48]:

$$P_h = 100 \times P_{atm} \times CR_{SE} \times \left(\frac{T_h + 273}{T_1 + 273}\right) \quad (35)$$

The SE pressure ratio is then calculated from the following equation:

$$R_{PSE} = \frac{P_h}{P_{atm} \times 100} \quad (36)$$

The maximum and minimum specific volumes (m^3/kg) are given as follows:

$$v_{max} = \frac{R \times (T_1 + 273)}{100 \times P_{atm}}, v_{min} = \frac{v_{max}}{CR_{SE}} \quad (37)$$

The mean effective pressure is estimated as [53]:

$$P_{mean} = \frac{P_{atm} \times (CR_{SE} + 1) \times (\tau + 1)}{4}, \tau = \frac{T_h + 273}{T_l + 273} \quad (38)$$

The piston volume can be obtained from the following equation [48]:

$$V_p = \frac{60 \times P_{SE}}{4\pi \times NOC_{SE} \times 1000 \times P_{mean} \times \vec{V}_{SE} \times F \times \frac{T_h - T_l}{T_h + T_l}} \quad (39)$$

Where F parameter is equal to 0.25–0.35.

The piston stroke is defined as [54]:

$$Stroke = \frac{V_p}{A_p}, A_p = \frac{\pi}{4} \times \left(D_p\right)^2 \quad (40)$$

The dish concentrator aperture area (projected area) is also determined as presented in Eq. (41) in [26]:

$$A_c = \frac{1000 \times P_{SE}}{I_s \times \eta_o} \quad (41)$$

The dish concentrator glass area (effective projected area or projected mirror area) is calculated by the following formula [10]:

$$A_{glass} = \frac{10}{11} \times A_c \quad (42)$$

The receiver aperture area is expressed as follows [55]:

$$A_r = \frac{A_c}{CR_{dish}} \quad (43)$$

The total number of dishes can be obtained as follows:

$$N_{dishes} = \frac{P_{tot}}{P_{SE}} \quad (44)$$

The total plant area is given as:

$$A_{tot,dish} = A_c \times N_{dishes} \quad (45)$$

2.3.4 Cost analysis model

The economic performance analysis of the hybrid system is calculated through estimating the LCOE and hourly cost using a set of equations developed in the MATLAB/Simulink® simulation tool. In this work, the batteries are assumed to be already fully charged from the grid. The general input includes the interest rate, plant lifetime, fixed charge rate, power cost or total installed cost per capacity and variable operating cost. Accordingly, the following assumptions have been made: plant lifetime is 25 years, the interest rate is 5%, the fixed charge rate is 0.098, variable operating cost for the turbine and the solar dish are 0 and 0.06 $/kWh, respectively, battery lifetime is 5 years, battery cost is 100 $/unit, turbine power cost is 1628 $/kWe, dish cost is 300 $/m^2, receiver cost is 185 $/kWe, engine cost is 370 to 400 $/kWe, and site cost is 2.2 $/m^2. Two economic indicators have been utilised to assess the economic performance of the system, namely the LCOE and the total hourly cost. Table 5 summarises the assumptions and methodologies related to the economic assessment.

Table 5: Cost analysis for all the units that have been considered in this study.

Economic parameters	
Interest rate, %	$i = 5$
Battery lifetime, year	$LT_b = 5$
Amortization factor, 1/y [50]	$A_f = \frac{i \times (1+i)^{LT_b}}{(1+i)^{LT_b} - 1}$
Plant lifetime, year	$LT_p = 25$
Fixed charge rate	$FCR = 0.098$
Batteries Bank	
Battery cost, $	$C_b = 100$
Variable operating cost of the batteries, $/kWh	$VOC_b = 0.07$ (Charging Electricity Price)
Direct capital cost of the batteries bank, $ [42]	$CC_b = 5 \times C_b \times NOB$, where NOB is No. of batteries.
Annual capital cost of the batteries bank, $/yr	$ACC_b = CC_b \times A_f$

Fixed operating cost of the batteries bank, $/y	$FOC_b = 0.05 \times CC_b$
Annual total cost of the batteries bank, $/yr	$ATC_b = ACC_b + FOC_b$
Hourly total cost of the batteries bank, $/hr	$HTC_b = \frac{ATC_b}{365 \times 24}$
Horizontal Axis Wind Turbine (HWT)	
Normalised capital cost, $/kWe	$POC = 1628$
Variable operating cost of the turbines, $/kWh	$VOC_t = 0$
Direct capital cost of the turbines, $ [12]	$CC_t = POC \times P_m$
Indirect capital costs of the turbines, $ [12]	$ICC_t = WTC + CTC + OCC \; or \; ICC_t = 0.86 \times CC_t$
where, the wind turbine cost share: $WTC = 0.65 \times CC_t$, construction cost share (Civil works): $CTC = 0.16 \times CC_t$, and other capital cost share: $OCC = 0.05 \times CC_t$	
Total capital cost of the turbines, $	$TCC_t = CC_t + ICC_t$
Annual capital cost of the turbines, $/yr	$ACC_t = TCC_t \times A_f$
Fixed operating cost of the turbines, $/yr	$FOC_t = FCR \times CC_t$
Annual total cost of the turbines, $/yr	$ATC_t = ACC_t + FOC_t$
Hourly total cost of the turbines, $/hr	$HTC_t = \frac{ATC_t}{24 \times 365}$
Solar Dish Stirling Engine (CPSD-SE)	
SE cost, $/kWe [56]	$CSE = 370 \; to \; 400\$/kW$
Receiver cost, $/kWe [56]	$CCR = 185\$/kW$
Dish concentrator cost, $/m^2 [56]	$CDC = 300\$/m^2$
Site cost is 2.2$/m^2 [56]	$SIC = 2.2\$/m^2$
Variable operating cost of the CPSD-SE, $/kWh	$VOC_{dish} = 0.06$
Direct capital cost of the CPSD-SE, $	$CC_{dish} = (COP \times P_{SE}) + ([CDC + SIC] \times A_c)$ Where $COP = CSE + CCR$
Indirect capital costs of the CPSD-SE, $	$ICC_{dish} = CPEC + CGC + OCC$
Where, the construction, procurement, and engineering cost share are calculated [11], [12]: $CPEC = 0.16 \times CC_{dish}$, contingency cost share: $CGC = 0.10 \times CC_{dish}$, other capital cost share: $OCC = 0.03 \times CC_{dish}$	
Total capital cost of the CPSD-SE, $	$TCC_{dish} = CC_{dish} + ICC_{dish}$
Annual capital cost of the CPSD-SE, $/yr	$ACC_{dish} = TCC_{dish} \times A_f$
Fixed operating cost of the CPSD-SE, $/yr	$FOC_{dish} = FCR \times CC_{dish}$
Annual total cost of the CPSD-SE, $/yr	$ATC_{dish} = ACC_{dish} + FOC_{dish}$
Hourly total cost of the CPSD-SE, $/hr	$HTC_{dish} = \frac{ATC_{dish}}{24 \times 365}$
Total Plant cost	
Total annual cost, $/y	$ATC_{tot} = ATC_b + ATC_t + ATC_{dish}$

Total hourly costs, $/h	$THC_{tot} = \frac{ATC_{tot}}{8760}$
Total variable operating costs, $/kWh	$VOC_{tot} = VOC_b + VOC_t + VOC_{dish}$
Total Levelised cost of energy, $/kWh [57], [58]	$LCOE_{tot} = \frac{THC}{Load\ factor \times P_{tot}} + VOC_{tot}$

3. Results and discussion

This chapter addresses the most important parameters that measure the system cost behaviour such as the plant size and area as well as several design conditions. As mentioned earlier, the system contains CPSD-SE, HWT and a battery bank, and each of these units should operate under the best-operating conditions at the location of the operation. Moreover, the chapter covers a comprehensive sensitivity analyses of the design variables of the sub-systems. Sensitivity analysis has been carried out (i) to determine how each system performance varies when small changes are applied to the selected design parameters and (ii) to deliver a better understanding of the impacts of different design criteria and the results from the technical analysis. Finally, the techno-economic performance of the system was tested in Jordan's weather conditions.

The developed model can inform real-life applications as it gives meaningful insights on the various design aspects of the incorporated individual components and how these parameters affect the size and the cost of the whole system. Therefore, the utilised methods and the developed model can serve as the basis to apply new designs in practical sites. As future research, the design model could be optimised to meet the constraints of real-life applications, such as targeted electricity demand.

3.1 Mathematical model validation

In this section, the obtained simulation results are compared with previous simulation studies and validated against experimental/manufacturer data. Due to lack of data for the integrated assembly, each component is validated individually and therefore it is reasonable to assume that the model for the integrated microgrid is reliable.

3.1.1 Wind turbine model validation

The simulation results of the HWT system are validated against commercial data derived from the Hofa wind farm in Irbid, Jordan [59]. The specifications of the farm are presented in Table 6 and this data was introduced as input to the model to allow comparisons. As depicted in Table 7, the comparison reveals a very good agreement between the developed model and the selected wind farm. It is shown that the power coefficient of the HWT unit of the developed model has errors of approximately 1.27% compared to the Hofa wind farm.

Table 6: Specifications of the selected models [59].

Description	Parameters	Hofa wind farm
General data	Country/zone	Jordan/Irbid
	Manufacturer	VESTAS
	Model	V27/225
	Number of Turbines	5
	Total nominal power	1125 kW
	Rated power	225 kW
Operating data	Cut-in wind speed	3.5 m/s
	Rated wind speed	14 m/s
	Cut-out wind speed	25m/s
	Rotor diameter	27 m
Rotor	Swept area	573 m^2
	Rotational speed	43 rpm
Generator	Generator efficiency	0.97
	load factor	0.95
Tower	Hub heights	33.5 m
Power curve	Wind speed	0-25 m/s
	Power coefficient	0.26

Table 7: Data validation results of the HWT model.

Description	The developed model	Hofa (Vestas V27/225)	Error (%)
Hub height	33.75	33.5	0.746
Rotor swept area	572.56	573	0.077
Power coefficient	0.2633	0.260	1.269
No. turbines	5	5	0

3.1.2 Solar dish model validation

The reliability of the CPSD-SE model was tested against findings from Buscemi et al. [27], under the same operating conditions. Table 8 lists the geometrical and operating parameters of the Ripasso dish-Stirling models used for validation [27]. The comparison shows that the developed model exhibits very good agreement with the experimental results of the Ripasso dish-Stirling, as indicated in Table 9. For example, the Stirling efficiency value has a deviation of approximately 9.34%. Overall, it can be concluded that the developed model is a reliable tool for simulating the performance of several CPSD-SE commercial prototypes.

Table 8: Design specifications of the 32 kWe Ripasso dish-Stirling system [27].

Specifications	**Unit**	**Quantity**
Ambient Temperature	^{o}C	25
Solar radiation	W/m^2	960
Stirling engine power	kWe	32
Working fluid	-	H_2
Receiver gas temperature	^{o}C	720
Engine speed	rpm	2300
No. of cylinders	-	4
Rim angle	degree	45^0
Generator efficiency	%	92.4
Receiver efficiency	%	94

Table 9: Data validation results of the CPSD-SE model.

Description	**The developed model**	**Experimental published data, Ripasso dish-Stirling** [27]	**Error (%)**
Stirling efficiency, %	34.99	32	9.344
Aperture diameter, m	12.71	12	5.917
Focal length, m	7.647	7.45	2.644
Optical efficiency, %	79.94	85	5.953
Number of solar dish/SE units	1	1	0

3.2 Technical sensitivity analyses

In general, sensitivity analysis is utilised to examine the system behaviour to changes to various uncertain parameters. Herein, the scope of this analysis is to investigate the effect

of varying several parameters on the performance of the system and to reduce the respective design limits as well as to identify optimum operational windows.

3.2.1 Concentrated parabolic solar dish Stirling engine

For the CPSD-SE, it is vital to study the effect of the design operating conditions of the system such as the area, dimensions and cost. These design aspects are considered based on real operating conditions that have been found in the literature [60]. The examined design parameters include the power delivered from the engine, working gases (H_e, Air, H_2, N_2, and CO_2), engine speed and dimensions, and mirrors and receiver material type. Based on the above aspects, the following assumptions have been made:

- Total power load range is in the range 25 kWe and 1 MWe.
- Rim angle for the dish is fixed at 37 deg.
- Top cycle temperature range is between 400 ^oC and 800 ^oC, while the ambient temperature (sink) range is between 15 ^oC and 35 ^oC.
- Operating hours are fixed at 10 hours, and the number of epochs is 1000.
- Dish power (one unit) ranges between 15 kWe and 30 kWe.
- The number of engine cylinders is 4 while the piston diameter is 5.5 cm and the running speed is 1800 rpm.
- The generator, receiver and mirror efficiencies are 95%, between 70 to 80% and 97%, respectively.

Figure 4 a-d represent the main input effective operating condition that impacts on the Stirling dish design aspects. Figure 4-a shows the random variation of the ambient temperature along 1000 epochs. The variation of the ambient temperature (sink temperature) influences the engine efficiency, compression ratio, and pressure ratio. Figure 4-b shows the incremental epochs of the top cycle temperature from 400 to 800 ^oC along 1000 epochs and it is observed that the top cycle temperature has a substantial effect on the engine geometry. Figure 4-c, d shows the variation of the total plant power and Stirling engine power along 1000 epochs. For the total power, it is assumed in this work to vary randomly as shown in Figure 4-c. However, for the Stirling engine power, the variation of the power values are assumed to increase from 15 up to 30 kWe along 1000 epochs.

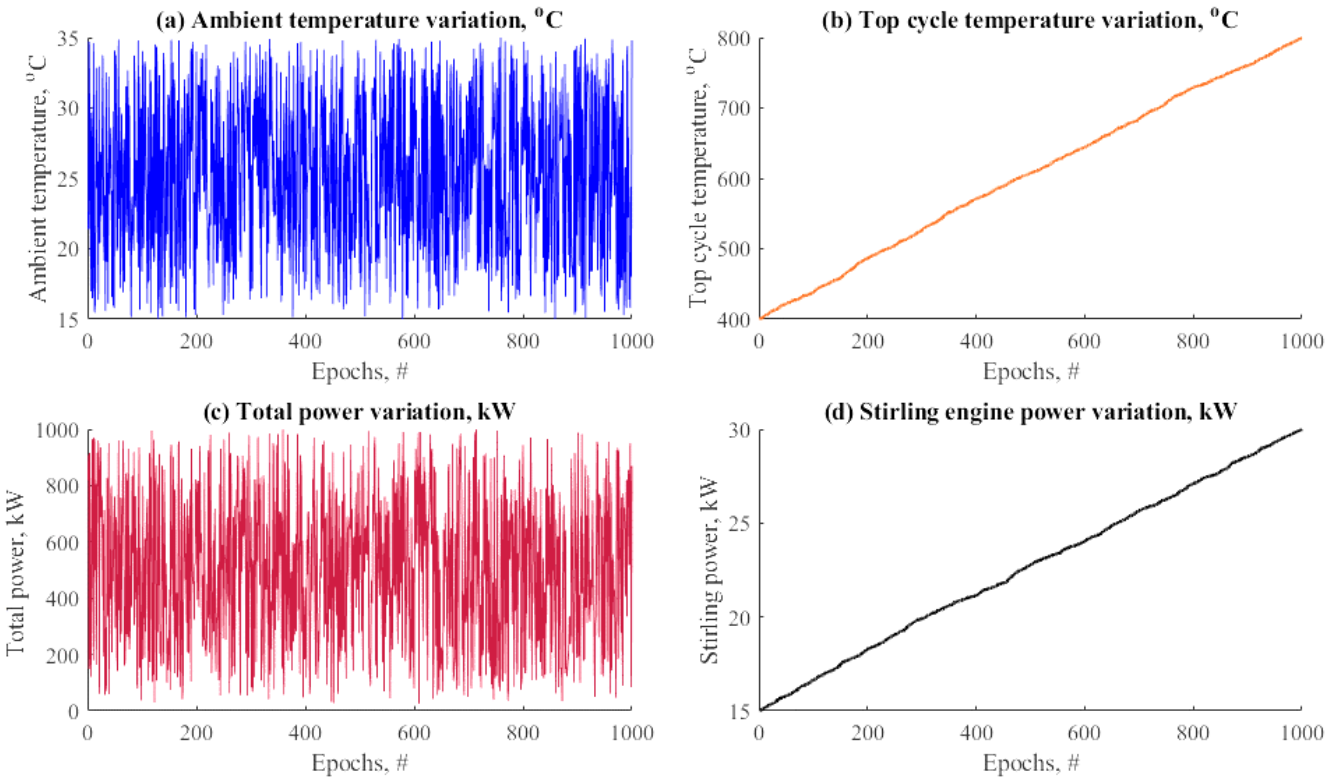

Figure 4. Main input data variations for the Stirling engine along 1000 epochs.

Figures 5 and 6 depict the technical results related to the solar dish Stirling component based on the input data variation that is shown in Figure 4. Figure 5 shows the results related to the dish concentration ratio (CR_{dish}), dish area, receiver area, total plant area, number of solar dishes and focal length. As depicted in Figure 5-a, by increasing the total load power results in a substantial increase in the CR_{dish} and also it affects the top cycle temperature (400-800 °C). It is typical for the designers to optimise the CR_{dish} point based on the total load power. A high CR_{dish} indicates that the load power is significantly increased. To illustrate this phenomenon, at a 400 kWe of load power, the CR_{dish} ranges between 480 and 550 and at a total load power of 600 kWe, the CR_{dish} is in the range of 700 to 785. The predicted dish area is shown in Figure 5-b where the behaviour substantially increases and fluctuates based on the variation in the top and sink temperatures. For instance, at 500 kWe of power, the dish area ranged between 90 to 100 m^2.

Figure 5-c shows that the receiver area decreases when the total power increases as a result of the increase of the dish concentration ratio ($CR_{dish}=A_c/A_r$). This decreases the receiver area, which leads to an expected decrease in the dish cost. The total plant area is shown in Figure 5-d and, as anticipated, the area increases with an increase in the power generation. Figure 5-e shows the number of dishes that should be employed in order to develop the required power for the load. For instance, at a 500 kWe load, the plant would use 20 to 25 dishes for the power generation. Also, the effect of the power generation on the solar dish geometry is observed in Figure 5-f. The focal length increases from 6.5 m to 9 m in an approximately linear manner with the generated power.

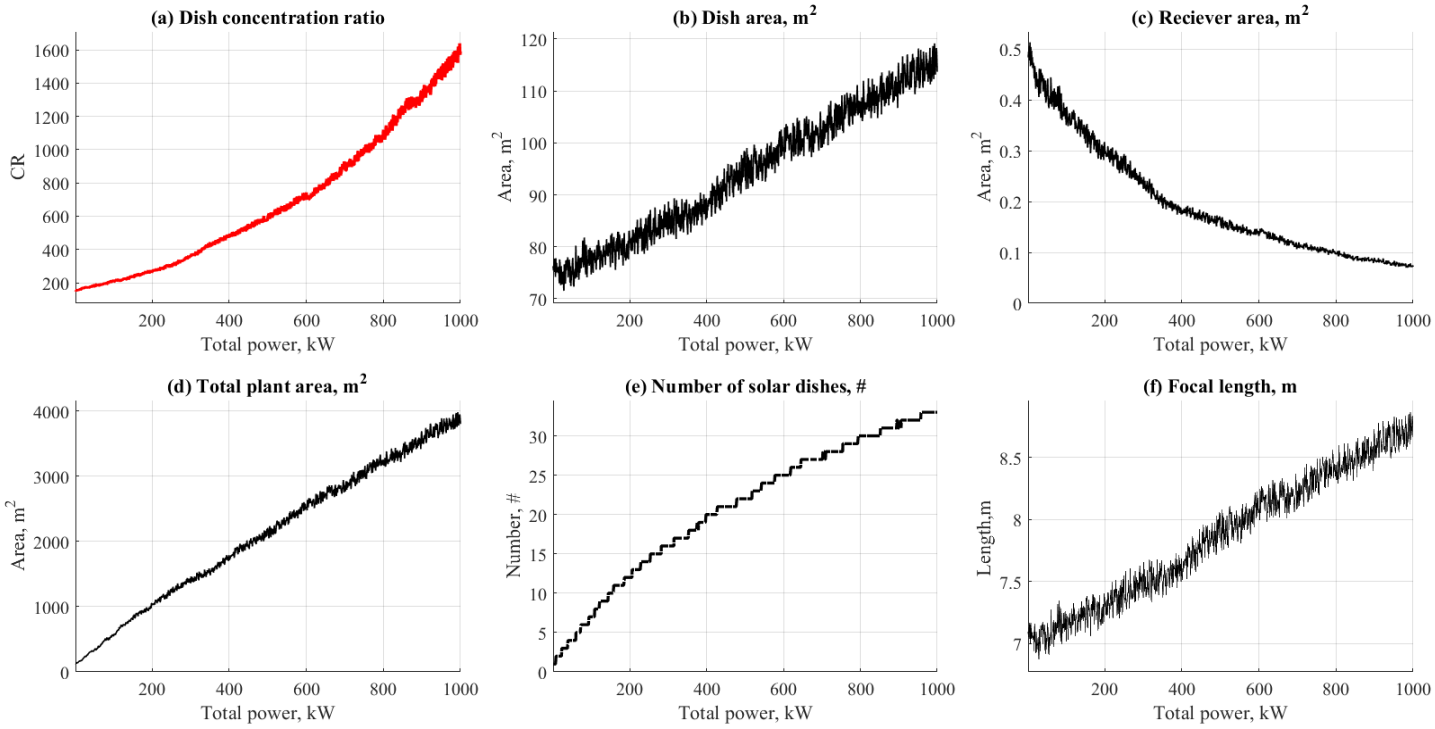

Figure 5. Design data results for the solar Stirling dish system based on the variation of load power, kWe.

Figure 6 shows the effect of the top cycle temperature and the engine power on the dish geometries and, as anticipated, by increasing the engine power then the area design parameters, such as the dish and receiver areas, also increase. The purpose of the analysis that is presented in Figure 6 aims at recognising the reduction and/or the expansion of the design limits and eventually allow the designers to compare between the employment of a large dish area and a low engine volume.

Figure 6-a shows that increasing the Stirling power from 10 kWe to 30 kWe requires an increase to the dish area from 20 to 120 m^2. The same trend is observed, as shown in Figure 6-b, to the receiver area where increasing the top cycle temperature requires a decrease in the dish area. However, increasing the power load on the Stirling dish requires an increase in the receiver area, as shown in Figure 6-b. The receiver area may increase from 0.1 to 0.8 m^2 based on the load power. Thus, it is now clear that the designers should better recognise the area limitations and/or the ranges based on the power delivered from the Stirling dish engine. Figure 6-c shows the effect of the top cycle temperature and engine power on the focal length, where increasing the top cycle temperature requires a slight decrease in the focal length. However, increasing the load power requires an increase in the focal length in line with the expected increase in the diameter of the solar dish. For the range of power from 10 kWe to 30 kWe, the focal length results in a range of 3.5 m to 8 m, respectively. Figure 6 shows that the obtained sensitivity results based on the top cycle temperature will assist the designer to optimise the selection between the engine power and the top engine temperature as a reflection on the dish area, receiver area and focal length.

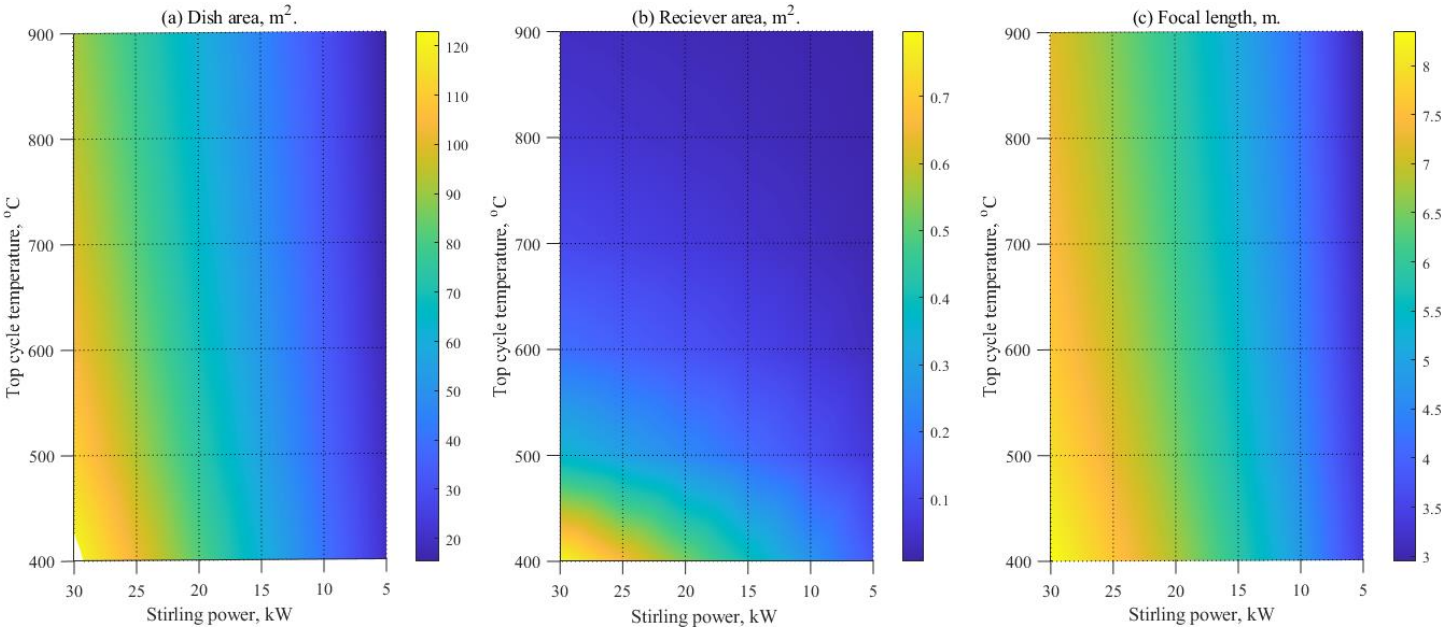

Figure 6. Stirling power and high cycle temperature effects on: (a) concentrator area, (b) Receiver area, and (c) Focal length.

Figure 7 shows the performance parameters that may be affected by the power load variation such as the efficiency, compression and pressure ratios, and engine dimensions. Figure 7-a shows that the engine efficiency increases as the total load power increases, reaching the maximum efficiency at the highest rate of the power load.

Similarly, an increasing upward trend is also evident in Figure 7-b, where the maximum plant efficiency is achieved when the rate of the power load is the highest. Figure 7-c shows that CO_2 achieves the highest compression ratio values, that range from 6 to 11, whereas He showed that the lowest compression ratio values lie between 2 and 3. For the diatomic gases, i.e. H_2 and the N_2, demonstrate similar compression ratios with air and these range from 4 to 6.

Generally, the use of CO_2 increases the solar Stirling performance rates and is highly recommended for the Stirling dish as a working gas regardless of the possible safety issues [48]. Figure 7-d shows the results of the use of different gases based on the pressure ratio, where high rates of compression and pressure ratios are much more favourable in increasing engine performance. The same behaviour was observed in Figure 7-d, which again confirms that CO_2 is extremely favourable for use as the working fluid once the pressure ratio values are in the range of 15 to 40 as the power load increases. As in the case for the engine compression in Figure 7-c, the diatomic gases are next with H_e showing the lowest values. As a consequence, the engine dimensions are required to increase, as shown in Figures 7-e and 7-f, which show the piston volume and stroke, respectively. As anticipated from the effect of the compression and pressure ratios, CO_2 exhibits lower values among the other working gases and this leads to a small dimension for the engine cavity. The total required volume under the operation of CO_2 ranged between 60 cm^3 and 80 cm^3 and the stroke was in the range of 2.5 cm up to 3 cm, which is quite small. In addition, diatomic gases, especially air, gave remarkable results in the range of 100 cm^3 to 120 cm^3 with respect to the volume and 4 cm to 5 cm with respect to the stroke.

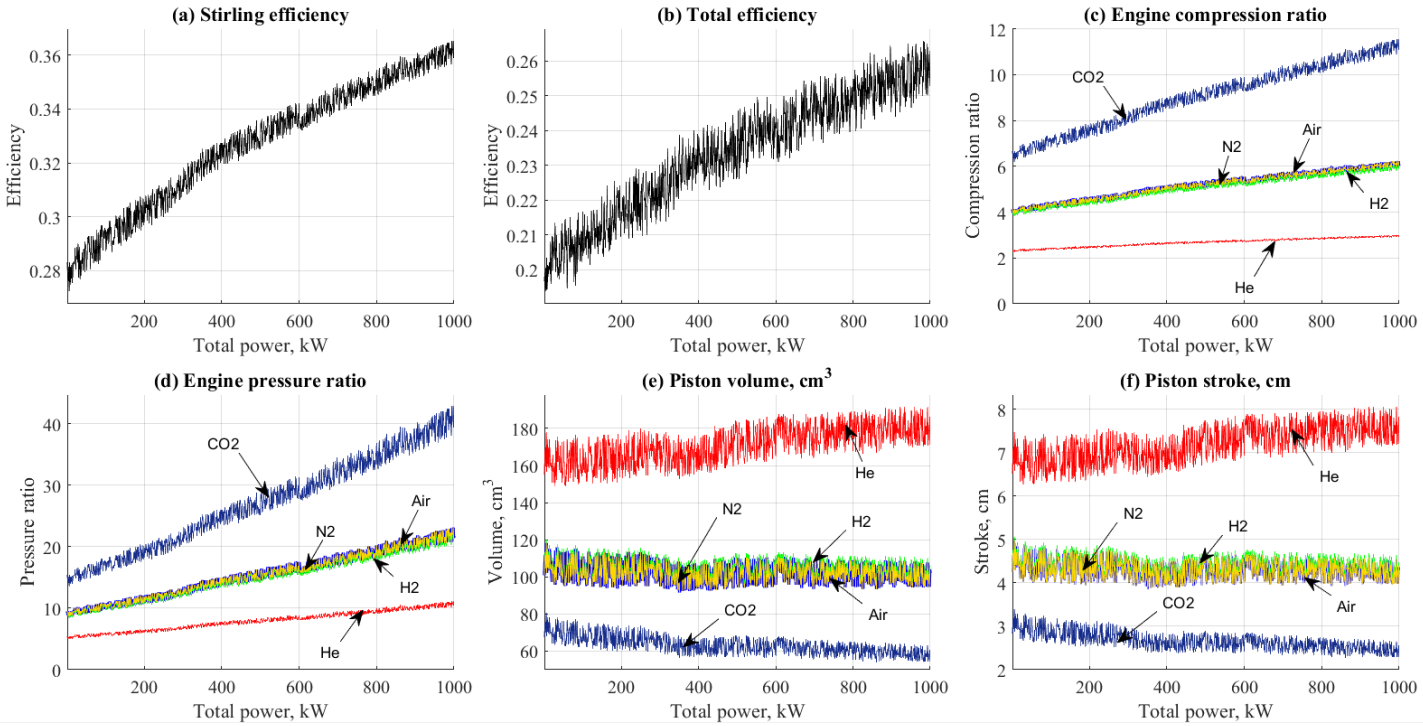

Figure 7. Design &Performance data results for the Stirling engine based on the total power variation.

3.2.2 Horizontal axis wind turbine

For a horizontal axis wind turbine (HWT), it is important to study the effect of various design operating conditions such as the total farm area, power coefficient of the turbine unit and total costs, $.

According to the above aspects, the following assumptions have been made:

- Total power load ranges between 500 kWe and 8000 kWe.
- The ambient temperature ranges between 15 °C and 25 °C.
- Operating hours are fixed at 10 hours and the number of epochs is 1000.
- Turbine power (one unit) ranges between 10 kWe and 500 kWe.

Figure 8-a shows the effect of the total farm power and the unit power on the power coefficient of the unit. Lower unit power (e.g., the 100 kWe) results in higher CP values that range between 0.2 and 0.24. At a high rate of the unit power, the CP decreases by almost 50% and therefore, it is evident that the use of 50 to 200 kWe module is preferred. Figure 8-b shows the result of the torque based on the power variation. As expected, increasing the power category increases the torque values. Figure 8-c shows the effect of the power (total and unit) on the farm area. For instance, at a total power of 8000 kWe and unit power 50-100 kWe, the farm area was found to be too large and equal to 0.6-0.8 km^2. For 8000 kWe

generation, the best option is to reduce the total farm area and to use module types with a range from 100 kWe up to 500 kWe. For power ranges below 2000 kWe, a module type of 100 kWe to 300 kWe is of considerable interest.

Figure 8-d shows the cost variation across various power ranges. Increasing the total farm power increases the total cost, as expected. For instance, at 8000 kWe of total power and a unit power of 1-50 kWe, the total cost was recorded as being extremely high (>2x10^7\$). However, at 8000 kWe of total power and a unit power range of 100 kWe to 200 kWe, the total cost was recorded to be in the mid-range (<1x10^7\$).

Based on the analyses that have been extracted from Figure 8, it is highly recommended to use a category of unit power in the range of 100 kWe to 300 kWe, especially in the case of a high range of total power generation (4000 kWe up to 8000 kWe). To reduce the total farm area, a unit power with a range of 300 kWe to 500 kWe should be considered. However, the power coefficient should be kept in mind to ensure that it should not be below a value of 0.2-0.24.

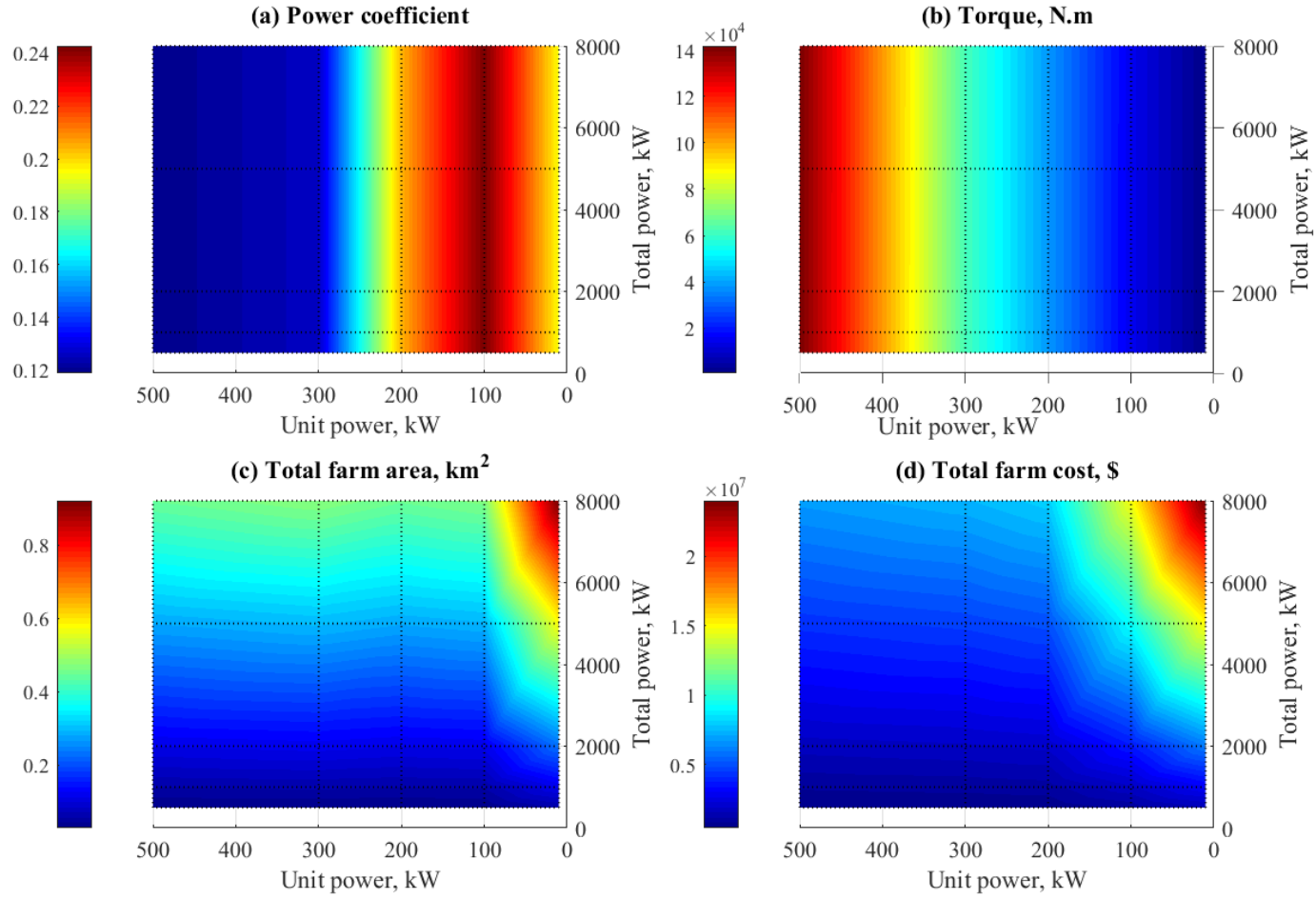

Figure 8. Data results for the HWT farm based on the total unit powers.

3.2.3 Battery bank

For the battery bank, the total number of the batteries required will affect the total battery cost and therefore it is important to control the battery voltage in order to control the cost of the battery. Figure 9 shows the data results of the battery bank according to the variation in the load power and it shows that increasing the load power increases all the parameters. For a depth of discharge equal to 80%, the battery efficiency is 75% and the battery voltage varies from 12 V up to 80 V; the results show that the total power increases almost linearly with the amount of energy as indicated in the Figures 9-a and 9-b. In addition, the number of batteries required increases substantially at a high load of power. For example, at 1500 kWe, the total number of batteries were calculated to be between 1800 and 1900 batteries. At the same time, the cost is increased significantly with respect to the increasing behaviour of the number of total batteries. Figure 9-d shows the increase in the total battery cost based on increasing the total power and this is related to the number of batteries. It is highly recommended that the designer selects the battery bank size based on cost considerations.

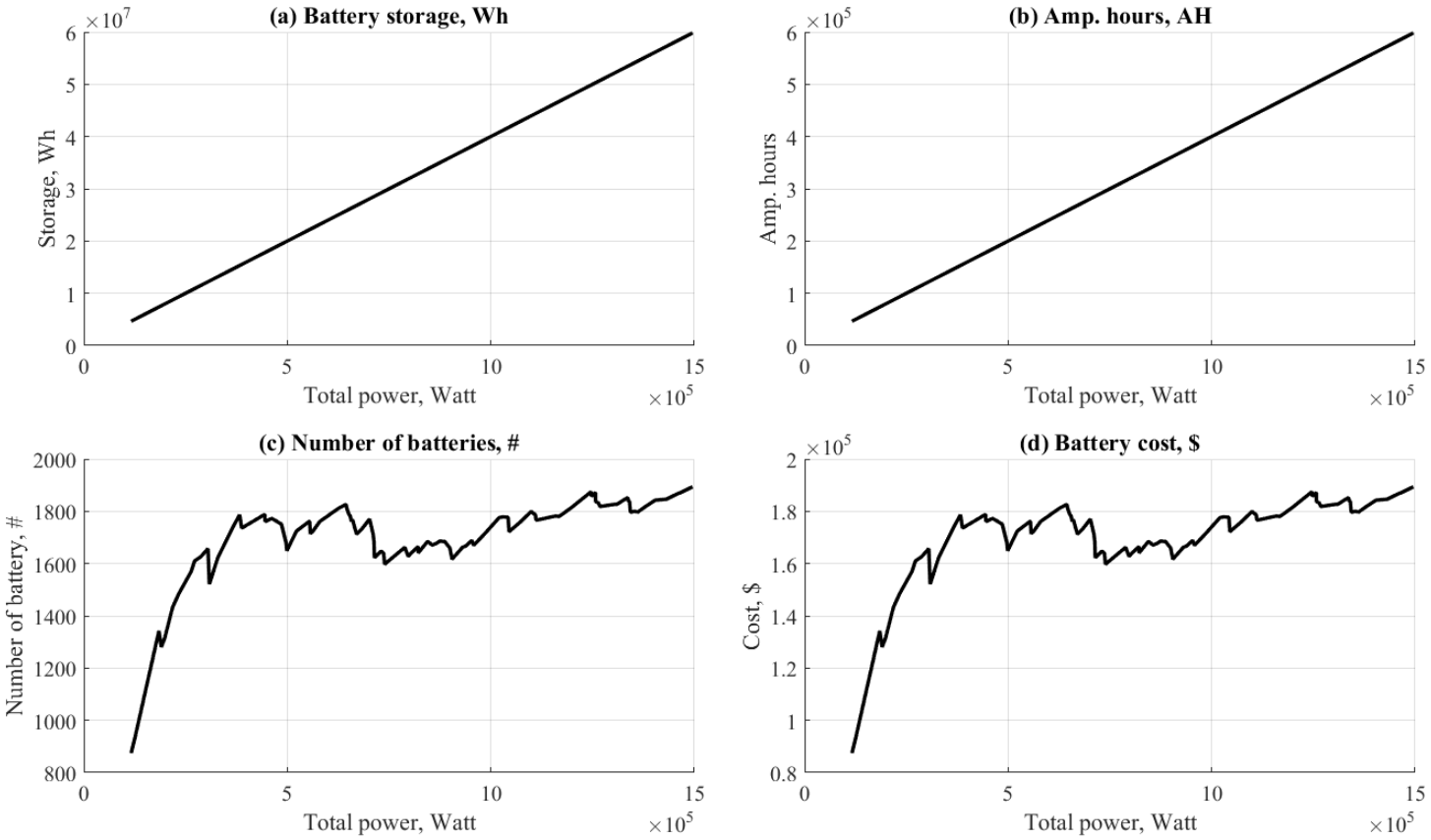

Figure 9. The results of the number of batteries required according to the load variation.

3.2.4 Control unit

The control unit is responsible for the load distribution between the system units. Figure 10 is the pseudo-algorithm that demonstrates the proposed control strategy for the operation management of the load distribution in the microgrid. Herein, the solar radiation and wind speed are the parameters that dictate the load distribution. Hence, the sub-system component operates according to the defined design limits of solar radiation and wind speed. The control unit makes a comparison between the input values and design limits of the meteorological variables. Solar radiation, I_s, ambient temperature, T_{amb}, air pressure, P_{air}, and operating hours, OH, are the main input operating conditions to the system. The input design parameters of each sub-system are listed in Tables 2-4 and the model after receiving the inputs calculates the design specifications of the system, as depicted in Figure 10. It is assumed that the solar radiation limit and wind speed are 500 W/m^2 and 1.5 m/s, respectively, at a fluctuated load power range from 100 kWe to 1500 kWe. If the solar radiation goes above the solar radiation limit, I_s >500 W/m^2, the signal would assign the Stirling dish to enter into service without the aid from the wind turbines and/or the battery bank. The Stirling dish keeps working as long as this condition is met. If the solar radiation goes below this limit and the average wind speed exceeds the wind limit, i.e. 1.5 m/s, then the wind turbines will enter into service. In any other case, the battery bank will serve the electrical demand.

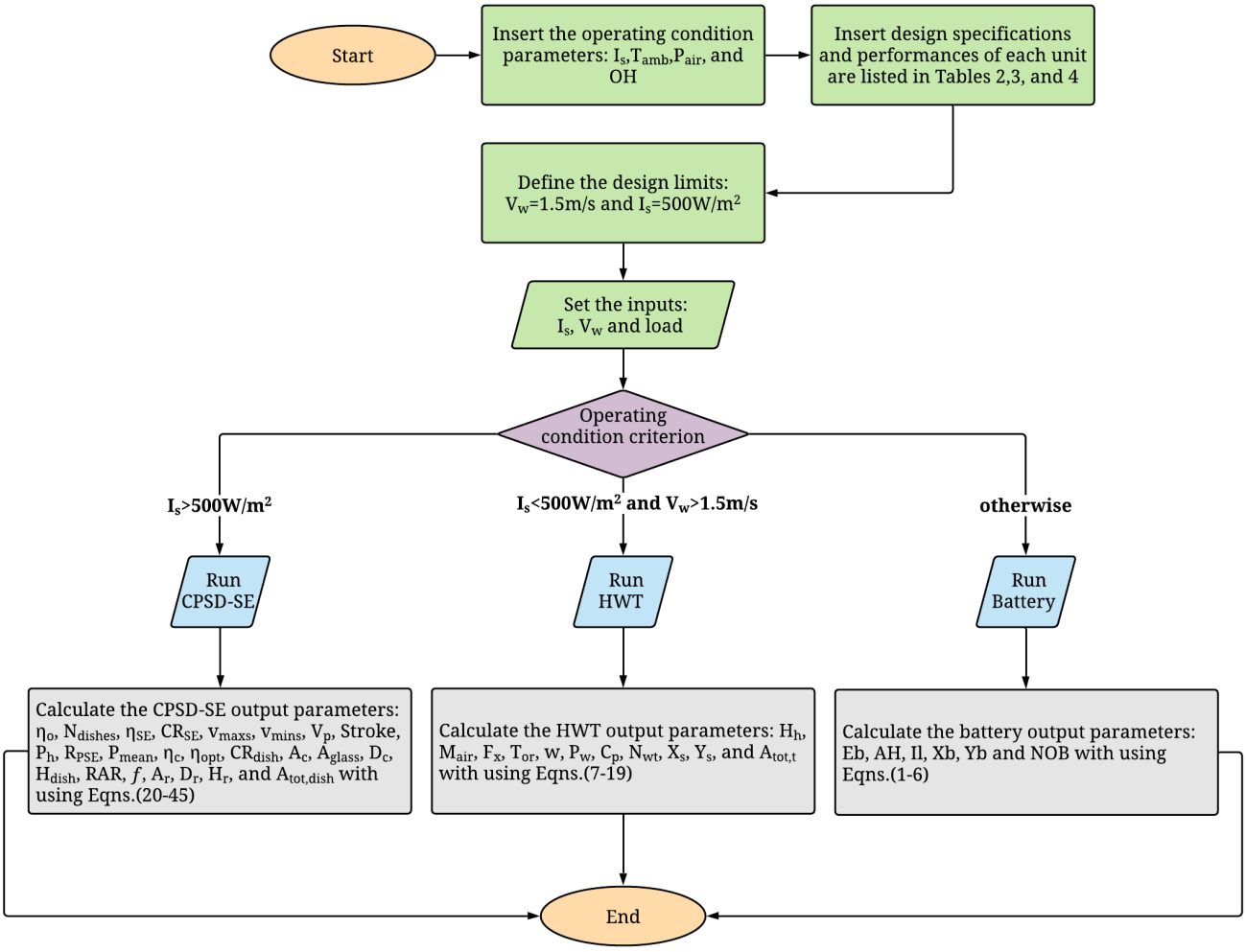

Figure 10. Flow chart of the control unit.

3.3 Implementation of the proposed system: A case study in Jordan

This section presents the results and findings of implementing the proposed energy system in two regions in Jordan. The system is designed to cover a load range from 100 kWe to 1500 kWe in order to simulate the operations under different conditions. The assessment has been performed by implementing the algorithm described in Figure 10 and using the parameters presented in Tables 2, 3 and 4. The assumed design considerations for the Jordan case are as follows:

- Time ranges:
  - 12 monthly epochs are considered as average measures throughout the year. A typical day in each month (21st day) is considered as a representative example for each of the 2 locations in Jordan.

- Solar and wind data for Jordan (2 locations):
  - Solar and wind data are obtained from Solargis™.
  - The locations are Madaba and Mafraq.
- Power range:
  - The load power on the system fluctuates, as shown in Figure 11, and has the same values for the two regions in order to facilitate comparisons. The power load is set in random fluctuation mode to approximate real-time operation.
- HWT system:
  - The 100 kWe module power category is selected.
  - The average ambient temperature is set at 25 ^{o}C for all locations.
  - The system operates at wind speeds greater than 1.5 m/s.
- Solar Stirling system:
  - CO_2 is the working gas.
  - Dish rim angle is 37 deg.
  - Top and low cycle temperature are 800 ^{o}C and 25 ^{o}C, respectively.
  - Dish power is 25 kWe.
  - Number of cylinders are 4.
  - The system operates at a solar flux greater than 500 W/m^2.
- Battery bank:
  - Depth of discharge is 0.8 and battery efficiency is 0.75.
  - Load voltage is 200 V and battery voltage is 80 V.

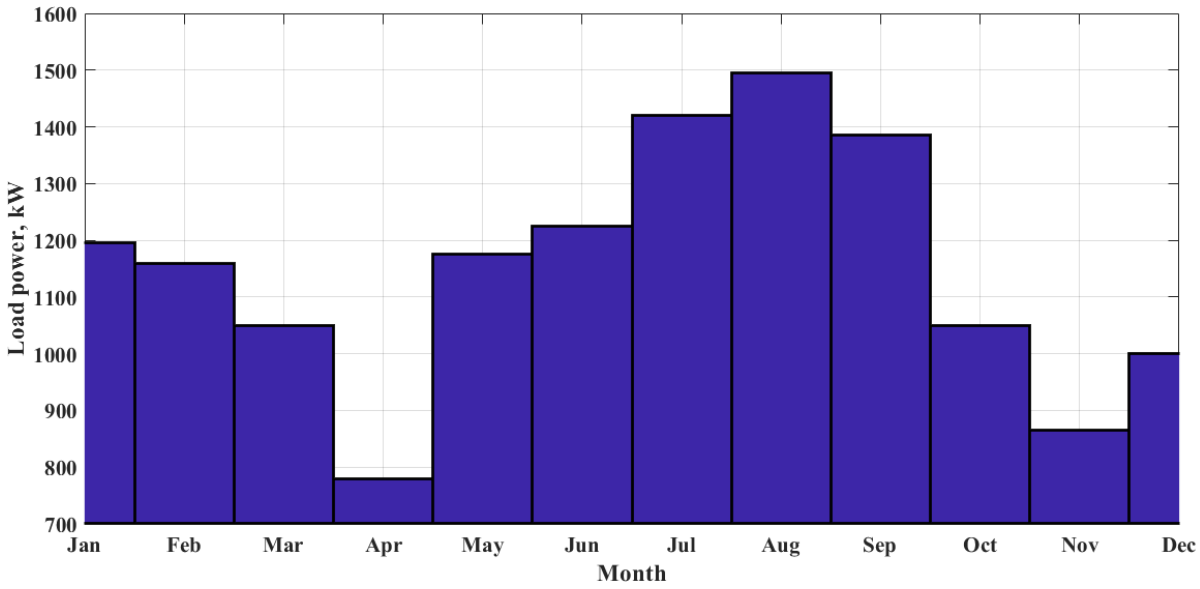

Figure 11. Power fluctuations per month as an example input.

The amount of wind speed and solar irradiation are very important design parameters in order to size a CPSD-SE/HWT for a specific region. The main purpose is to calculate a proper configuration of the selected system, which is able to sufficiently generate the electricity continuously throughout the year. Figures 12-a to d present the annual wind speed and solar radiation data (on a monthly resolution) in Madaba and Mafraq. Figures 12-a and 12-c show the meteorological data results at the location of Madaba related to the wind speed and solar radiation variation. The speed is recorded as being significantly low since it is within the range of 1.4 m/s to 2 m/s. This indicates that there is much more use of solar energy, especially with the very good conditions of solar radiation, as shown in Figure 12-c which clearly shows that the average measured values of the direct normal irradiation are approximately 1055 W/m^2. In addition, it is clear that throughout the summer season that the wind and solar energy simultaneously have their maximum values. Consequently, it is noted that, generally, the generated power is the highest in the summer season. Figures 12-b and 12-d present the findings for Mafraq. As shown in Figure 12-b, the wind speed is recorded as being very high during the summer and winter periods, i.e. in the range of 2.5 m/s to 5.5 m/s. The solar

radiation is also recorded as high in the summer and in winter periods and range between 615 W/m^2 to 830 W/m^2 (see Figure 12-d).

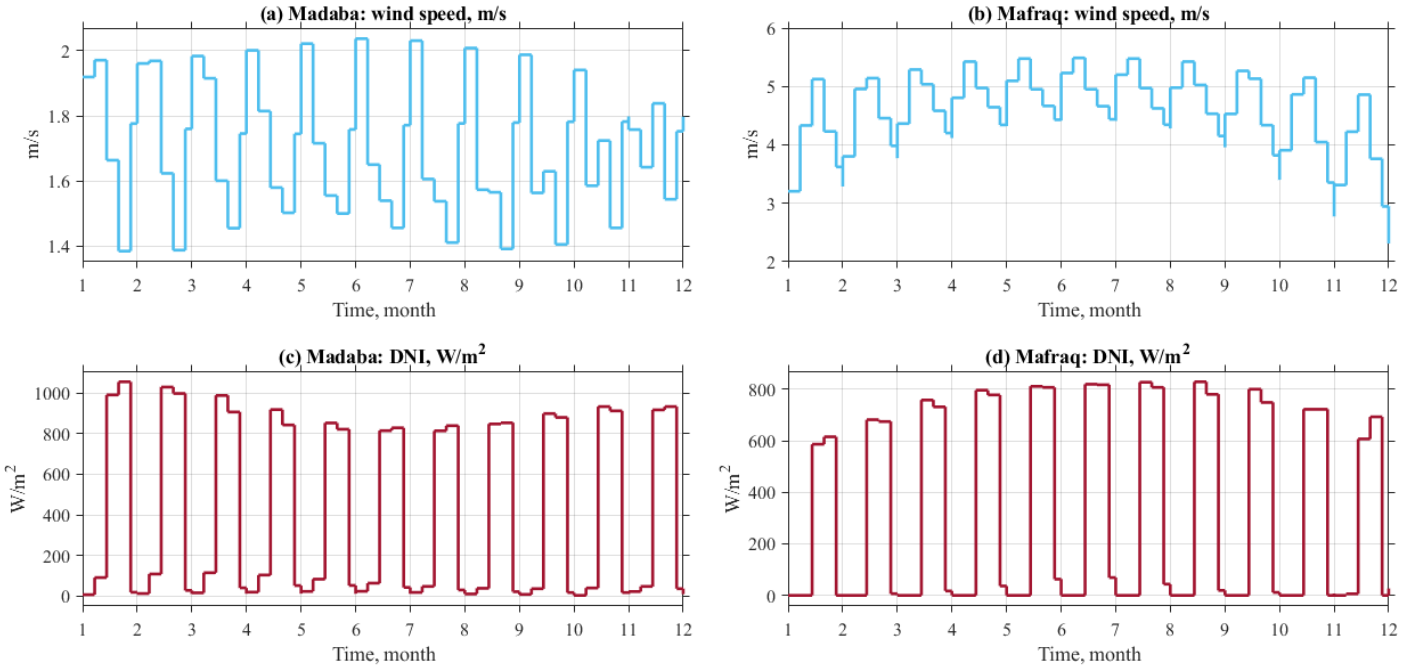

Figure 12. Wind speed and solar radiation profiles at selected locations throughout one year.

Figure 13 shows the generated power from each system component throughout one year for the investigated locations (Madaba & Mafraq). The behaviour of Figure 13 reflects the fluctuation in operating conditions (solar & wind) along 12 months. As shown in Figure 13-a, most of the power generation throughout the year in Madaba is dominated by the solar dish where the empty epochs occur due to the solar radiation power absence. Similarly, as depicted in Figure 13-b (Mafraq), the power generation along the year would be mostly covered by solar dish and the lack of solar power should be compensated by the existence of wind and/or battery as shown in Figure 13-d and Figure 13-f. Figure 13-c (Madaba) depicts that the HWT contribution is relatively high along the whole year and mostly occurs during the summer months and thus the battery operation is almost not utilised due to the abundant harmonic coexistence of solar and wind energy (see Figure 13-e). On the other hand, in Mafraq the battery bank has a high rate of operational time, as shown in Figure 13-f mainly due to lack of sufficient wind energy available. It appears then that the weather conditions in Madaba are more suitable for the implementation of the proposed system since less battery energy is required.

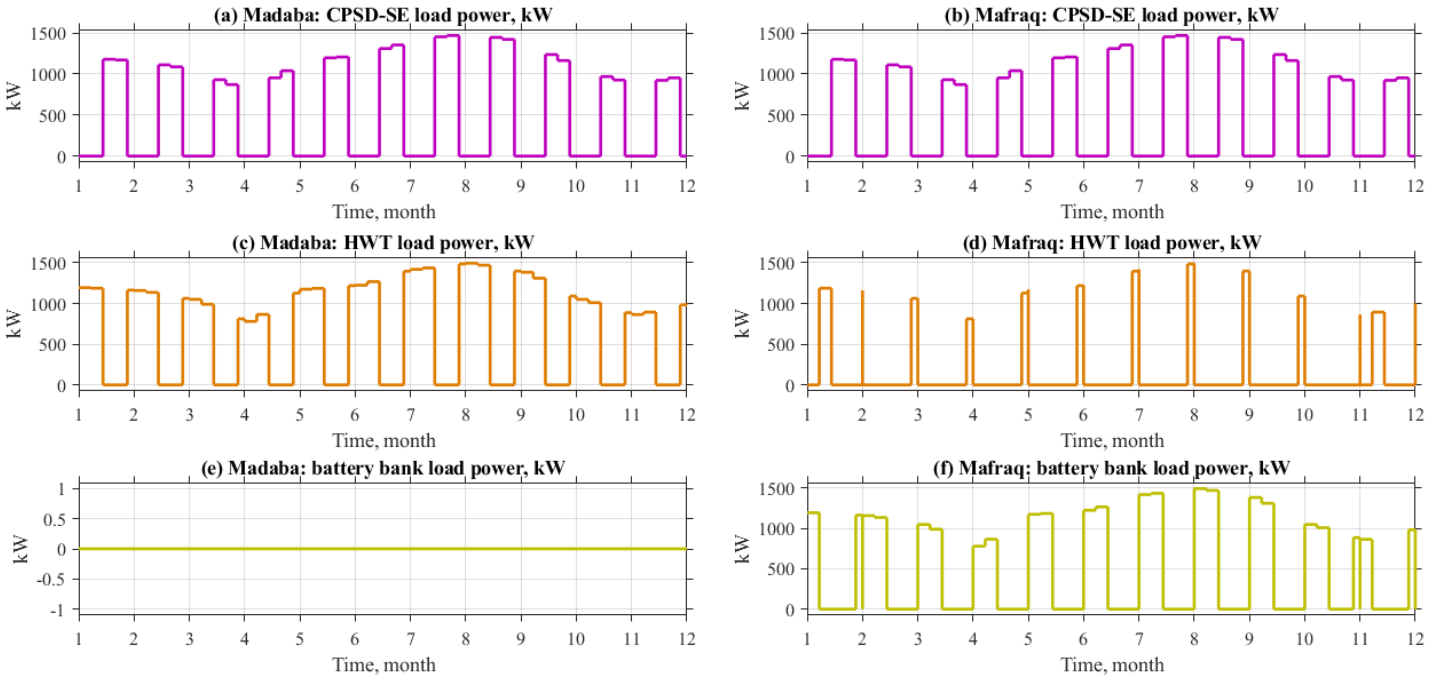

Figure 13. Monthly data results at the Madaba and Mafraq locations based on the variation of the load, solar radiation, and wind speed.

Additionally, a preliminary economic assessment has been conducted in order to give an initial estimation of the economic performance of the system. In a future work, detailed economic assessment along with the performance modelling will be carried out. Figure 14 presents the cost results for both locations; Mafraq and Madaba. In general, the LCOE in Madaba lies between 0.1307 and 0.1361 $/kWh and the hourly costs are found to be in the range between 0.9245 and 4.274 $/h, while the LCOE in Mafraq lies between 0.1307 and 0.1483 $/kWh and the hourly costs are found in the range between 0.9245 and 24.64 $/h. The average hourly costs across one year are 3.0373 $/h and 4.5070 $/h for Madaba and Mafraq, respectively. Madaba appears to have significantly lower hourly costs and this is due to its greater solar potential which eliminates the necessity for the use of batteries. The Mafraq location has a lower solar potential and frequent use of batteries is required, and consequently these results in the higher costs.

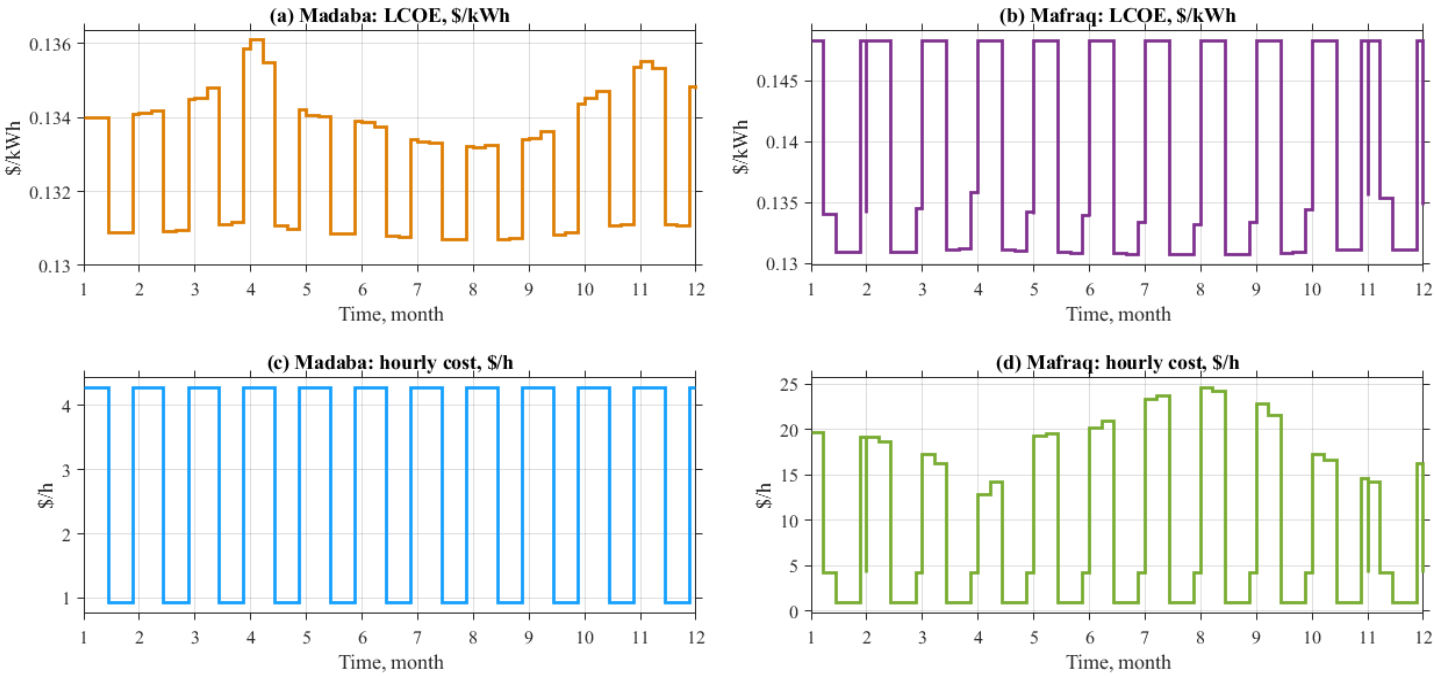

Figure 14. Average monthly LCOE and hourly costs of the proposed system.

Tables 10 and 11 present an LCOE comparison of the investigated system with different types of stand-alone, as well as hybrid, renewable energy technologies that have been found in the literature. In particular, Table 10 indicates a comparison of economic results related to stand-alone solar technologies and it shows that the CPSD-SE is the most cost-effective solar system. The results reveal that the estimated LCOE of the CPSD-SE (0.0601 $/kWh) is the lowest compared with other solar power plants that have been implemented in the MENA region.

Table 10. LCOE comparison of the CPSD-SE and other solar power plants.

Solar Technology	Reference	Location	Software	Rated power (MWe)	LCOE ($/kWh)
CPSD-SE	Present study	Jordan	MATLAB	1.5	0.0601
Parabolic Trough	[61]	Kuwait	SAM	50	0.1507
Power Tower	[62]	Iran	SAM	100	0.1130
Liner Fresnel	[63]	Algeria	SAM	50	0.1382
PV	[64]	Oman	HOMER	10	0.085

Moreover, a comparison of the LCOE between the proposed hybrid system (the whole assembly) and other hybrid renewable assembles has been also conducted. As shown in Table

11, the CPSD-SE/HWT is highly competitive with other HRES. Even if the CPSD-SE/battery assembly [21] has a lower LCOE, the proposed CPSD-SE/HWT/battery possess higher reliability and hence it is more suitable for microgrid applications. To illustrate this point, on using the hybrid CPSD-SE/HWT/battery on a medium-power scale (>1 MWe) would mitigate the use of batteries and therefore, the LCOE would decrease. Moreover, the proposed system has a lower LCOE than the CPSD-SE/biomass. As a result, the CPSD-SE/HWT configuration is economically competitive and can provide a sustainable solution for microgrid applications. It can be, also, observed that the developed system is the most cost-effective solar and wind hybrid system. Most importantly, the LCOE of the present model is lower than the typical PV/wind system, as clearly shown in Table 11. It should be noted that in the LCOE calculation, previous studies might have considered different assumptions for the lifetime, discount rate and capacity factor and different methodologies for the capital expenses (CAPEX) and operating expenses (OPEX) calculations. This is in general a limitation that exists in any techno-economic assessment that is available in the literature and this hinders effective comparisons between the different technologies. Nevertheless, it is evident that the hybrid CPSD-SE/HWT/battery is a competitive and a cost-effective integrated option when compared with other renewables for implementation in arid/semi-arid regions. Overall, the LCOE provides a good indication to the policy makers and useful information in comparing the feasibilities of different renewable energy technologies.

Table 11. Comparison between the proposed CPSD-SE/HWT system and other stand-alone hybrid renewable technologies in terms of LCOE.

Hybrid system	**Reference**	**Location**	**Software**	**Rated power (kW_e)**	**LCOE ($/kWh)**
CPSD-SE/HWT/battery	Present study	Jordan	MATLAB	1500	0.130
CPSD-SE/battery	[21]	Jordan	SAM	9.5	0.1150
CPSD-SE/ biomass	[30]	China	SAM	850	0.1617
CPSD-SE/HWT	Present study	Jordan	MATLAB	1500	0.13
PV/WT	[65]	Iran	HOMER and MATLAB	6.6	0.167

PV/WT	[66]	Turkey	RET-Screen	6	0.156
CSP/WT	[67]	Morocco	MATLAB	50,000	0.264
CSP/PV/WT	[67]	Morocco	MATLAB	50,000	0.183

4. Conclusions

A novel integrated solar and wind power generation system has been presented, investigated and analysed in terms of the design, size and cost aspects. The system comprises a solar dish Stirling engine and a horizontal axis wind turbine coupled with a battery bank that can generate electricity for medium-scale applications (e.g., residential buildings) in arid and semi-arid regions. A CPSD-SE has been used as the prime mover and during the periods of no or limited sunlight, a HWT and battery bank have been employed for back-up electricity procurement. Further, the techno-economic performance of a 1500 kWe CPSD-SE/HWT system was investigated in two locations in Jordan (Mafraq and Madaba). For the design aspects, a steady-state mathematical model has been developed to conduct a detailed techno-economic assessment. The proposed mathematical model has been validated against relevant experimental and manufacturer data separately for each system component and in general the model is in very good agreement with the actual data. The simulation process has been executed in the MATLAB/Simulink® software and the results show that:

- The performance of the CPSD-SE at 1000 kWe is improved with the high-top cycle temperature at 800 ^{o}C, high dish concentration ratio of 1600, small receiver area of 0.1 m, large dish diameter of 115 m^2, large focal length of 8.9, high pressure and compression ratio of 40 and 11, respectively, low wind speed of 1.4 to 2 m/s and 2.5 to 5.5 m/s, and high DNI of 1055 W/m^2 and 830 W/m^2 at Madaba and Mafraq, respectively.
- CO_2, N_2, H_2, H_e and air were tested as SE working fluids, and compared to each other with respect to the efficiency, compression ratio, pressure ratio, and engine dimensions. Based on the findings, CO_2 appears to be the most suitable working fluid for the SE and provides the highest output power load as it has the highest pressure and compression ratios, i.e. 40 and 11, respectively. Consequently, the engine efficiency can be as high as 37%.
- At 1500 kWe, a HWT module of 100 kWe is found to be more suitable for the operation in terms of cost, torque, and farm size. In addition, the power coefficient of the HWT is

in an acceptable range of 0.2 to 0.24 and the total number of batteries required to cover this load is between 1800 and 1900.

For the operating conditions aspects, the techno-economic assessment revealed the following:

- Solar and wind meteorological data at the selected locations have been included in the cost model. The solar radiation yields different results for both locations. The peak solar radiation at Mafraq has been recorded in August with about 830 W/m^2, while the maximum DNI value at Madaba has been recorded in January with about 1055 W/m^2. Mafraq recorded greater wind speed values than Madaba, i.e. 2.5 to 5.5 m/s and 1.4 to 2 m/s, respectively and wind speed peaks are observed during the summer at both locations.
- The preliminary economic evaluation revealed that the hybrid CPSD-SE/HWT is competitive, and the LCOE lies between 0.1307 $/kWh and 0.1361 $/kWh in Madaba and between 0.1307 $/kWh and 0.1483 $/kWh in Mafraq. Also, Madaba records moderately lower hourly costs due to its favourable solar and wind profiles compared to Mafraq and the resulting average hourly costs across one year are 4.507 $/h and 3.037 $/h for Mafraq and Madaba, respectively.
- The peak power generated by the CPSD-SE/HWT is about 1500 kWe and it is observed during the summertime in both locations.

From this investigation, it is clear that the HWT/CPSD-SE system design aspects (area, dimension, cost, etc.) are affected by the operating conditions and the working fluid selection. In general, the system can advantageously compete against concentrated solar power and/or photovoltaic systems in the case of medium scale distributed power generation systems.

Acknowledgement

The authors would like to acknowledge Al al-Bayt University and the Oman Ministry of Higher Education for their valuable financial support.

Nomenclature

A	Cross-sectional area, m^2
ACC	Annual capital cost, $/yr
A_{dish}	Dish concentrator aperture area, m^2

AH_b	Battery amp-hours, Ah
A_r	Receiver aperture area, m^2
A_r	Rotor swept area, m^2
ATC	Annual total cost, $/yr
A_{tot}	Farm total area, km^2
C_b	Battery cost, $
CC	Capital cost, $
CCR	Cavity receiver cost, $/kWe
CC_t	Capital cost of the turbines, $
CDC	Dish concentrator cost, $/$m^2$
COP	Total direct cost per capacity, $/kWe
C_P	Power coefficient
CPEC	Construction, procurement and engineering cost share, $
CPSD-SE	Concentrated parabolic solar dish Stirling engine
CR_{dish}	Dish concentration ratio, %
CSE	Stirling engine and alternator cost, $/kWe
CTC	Contingency cost share, $
C_v	Specific heat capacity at constant volume, kJ/kg.^{o}C
D	Diameter, m
DOD	Battery depth of discharge
E_b	Battery storage capacity, Wh
f	Focal length, m
FCR	Fixed charge rate
F_x	Axial force, kN
HBATC	Hourly total cost of the batteries, $/hr
H_{dish}	Dish height, m
H_h	Hub height, m
HTC	Hourly total cost, $/hr
i	Interest rate, %
I_b	Battery current, A
ICC	Indirect capital costs, $

I_l	Load current, A
I_s	Solar Radiation, W/m^2
$LCOE_b$	Levelised cost of energy, $/kWh
LT_b	Battery lifetime, year
LT_p	Plant life time, year
m	Mass flow rate, kg/s
M_{air}	Air mass flow rate, kg/s
NOB	Number of batteries
NOC	Number of cloudy days factor, day
NOC_{SE}	Number of Stirling engine cylinders
NOD	Total number of dishes
N_{wt}	Number of HWT
OCC	Other capital cost share, $
OH	Operating hours, hour
P	Pressure, bar
P_{mean}	Mean effective pressure, bar
POC	Normalised capital cost or total installed cost per capacity, $/kWe
P_{SE}	Stirling engine power, kWe
P_{tot}	Total plant power, kWe
P_w	Required wind power, kWe
R	Specific gas constant, kJ/kg^{o}C
RAR	Rim angle ratio
R_{PSE}	Stirling pressure ratio
SIC	Site cost, $/m^2.
T	Temperature, ^{o}C
T_{amb}	Ambient temperature
TCC	Total capital cost, $
T_{or}	Rotor torque, N.m
TPC	Total plant costs, $
V	Volume, cm^3
v	Specific volume, m^3/kg

V_b	Battery voltage, V
V_l	Load voltage, V
v_{max}	Maximum specific volume, m^3/kg
$\vec{V}_{SE}$	Stirling engine speed, rpm
VOC	Variable operating cost, $/kWh
WTC	Wind turbine cost share, $
X_s	Spacing in wind direction, m
Y_s	Spacing cross the wind direction, m
η_c	Concentrator efficiency, %
η_{gen}	Generator efficiency, %
η_{SE}	Stirling engine efficiency, %
ρ_m	Mirror reflectance
ψ_r	Rim angle, degrees

Subscripts:

a	Actual
amb	Ambient
atm	Atmospheric
b	Battery
c	Dish concentrator
dish	Dish
gen	Generator
h	High
i	inlet
l	Low
o	Out
opt	Optical
p	Piston
r	Cavity receiver
SE	Stirling engine
t	Turbine
tot	Total

Greek:

Γ	Intercept factor
ε	Effective emissivity
η	Efficiency
ψ	Angle

References

[1] Z. Wang, W. Yang, F. Qiu, X. Zhang, and X. Zhao, “Solar water heating: From theory, application, marketing and research,” *Renewable and Sustainable Energy Reviews*, vol. 41, pp. 68–84, 2015, doi: 10.1016/j.rser.2014.08.026.

[2] S. A. Kalogirou, *Solar thermal collectors and applications*, vol. 30, no. 3. 2004. doi: 10.1016/j.pecs.2004.02.001.

[3] V. v. Tyagi, S. C. Kaushik, and S. K. Tyagi, “Advancement in solar photovoltaic/thermal (PV/T) hybrid collector technology,” *Renewable and Sustainable Energy Reviews*, vol. 16, no. 3, pp. 1383–1398, 2012, doi: 10.1016/j.rser.2011.12.013.

[4] A. Kribus, D. Kaftori, G. Mittelman, A. Hirshfeld, Y. Flitsanov, and A. Dayan, “A miniature concentrating photovoltaic and thermal system,” *Energy Conversion and Management*, vol. 47, no. 20, pp. 3582–3590, 2006, doi: 10.1016/j.enconman.2006.01.013.

[5] X. Lu, K. Zhou, and S. Yang, “Multi-objective optimal dispatch of microgrid containing electric vehicles,” *Journal of Cleaner Production*, vol. 165, pp. 1572–1581, 2017, doi: 10.1016/j.jclepro.2017.07.221.

[6] R. Kumar, R. A. Gupta, and A. K. Bansal, “Economic analysis and power management of a stand-alone wind/photovoltaic hybrid energy system using biogeography based optimization algorithm,” *Swarm and Evolutionary Computation*, vol. 8, pp. 33–43, Feb. 2013, doi: 10.1016/j.swevo.2012.08.002.

[7] R. Belfkira, L. Zhang, and G. Barakat, “Optimal sizing study of hybrid wind/PV/diesel power generation unit,” *Solar Energy*, vol. 85, no. 1, pp. 100–110, 2011, doi: 10.1016/j.solener.2010.10.018.

[8] A. Zurita *et al.*, “Techno-economic evaluation of a hybrid CSP + PV plant integrated with thermal energy storage and a large-scale battery energy storage system for base generation,” *Solar Energy*, vol. 173, no. August, pp. 1262–1277, 2018, doi: 10.1016/j.solener.2018.08.061.

[9] Y. F. Nassar *et al.*, “Dynamic analysis and sizing optimization of a pumped hydroelectric storage-integrated hybrid PV / Wind system : A case study,” *Energy Conversion and Management*, vol. 229, no. November 2020, p. 113744, 2021, doi: 10.1016/j.enconman.2020.113744.

[10] L. S. Mendoza Castellanos *et al.*, “Experimental analysis and numerical validation of the solar Dish/Stirling system connected to the electric grid,” *Renewable Energy*, vol. 135, pp. 259–265, 2019, doi: 10.1016/j.renene.2018.11.095.

[11] H. M. Ali, “Recent advancements in PV cooling and efficiency enhancement integrating phase change materials based systems – A comprehensive review,” *Solar Energy*, vol. 197, no. June 2018, pp. 163–198, 2020, doi: 10.1016/j.solener.2019.11.075.

[12] I. R. E. Agency, “Renewable Energy Technologies: Cost Analysis Series,” 2012. doi: 10.1016/B978-0-12-812959-3.00012-5.

[13] U. Desideri, F. Zepparelli, V. Morettini, and E. Garroni, “Comparative analysis of concentrating solar power and photovoltaic technologies: Technical and environmental evaluations,” *Applied Energy*, vol. 102, pp. 765–784, 2013, doi: 10.1016/j.apenergy.2012.08.033.

[14] N. Komendantova and A. Patt, “Employment under vertical and horizontal transfer of concentrated solar power technology to North African countries,” *Renewable and Sustainable Energy Reviews*, vol. 40, pp. 1192–1201, 2014, doi: 10.1016/j.rser.2014.07.072.

[15] F. Report, “Trans-Mediterranean Interconnection for Concentrating Solar Power,” 2006.

[16] B. Shboul *et al.*, “A new ANN model for hourly solar radiation and wind speed prediction : A case study over the north & south of the Arabian Peninsula,” *Sustainable Energy Technologies and Assessments*, vol. 46, no. October 2020, p. 101248, 2021, doi: 10.1016/j.seta.2021.101248.

[17] S. Y. Wu, L. Xiao, Y. Cao, and Y. R. Li, “A parabolic dish/AMTEC solar thermal power system and its performance evaluation,” *Applied Energy*, vol. 87, no. 2, pp. 452–462, 2010, doi: 10.1016/j.apenergy.2009.08.041.

[18] A. Poullikkas, G. Kourtis, and I. Hadjipaschalis, “Parametric analysis for the installation of solar dish technologies in Mediterranean regions,” *Renewable and Sustainable Energy Reviews*, vol. 14, no. 9, pp. 2772–2783, 2010, doi: 10.1016/j.rser.2010.07.021.

[19] M. Abbas, B. Boumeddane, N. Said, and A. Chikouche, “Dish Stirling technology: A 100 MW solar power plant using hydrogen for Algeria,” *International Journal of Hydrogen Energy*, vol. 36, no. 7, pp. 4305–4314, 2011, doi: 10.1016/j.ijhydene.2010.12.114.

[20] J. Ruelas, N. Velázquez, and J. Cerezo, “A mathematical model to develop a Scheffler-type solar concentrator coupled with a Stirling engine,” *Applied Energy*, vol. 101, pp. 253–260, 2013, doi: 10.1016/j.apenergy.2012.05.040.

[21] K. S. Reddy and G. Veershetty, “Viability analysis of solar parabolic dish stand-alone power plant for Indian conditions,” *Applied Energy*, vol. 102, pp. 908–922, 2013, doi: 10.1016/j.apenergy.2012.09.034.

[22] G. C. Bakos and C. Antoniades, “Techno-economic appraisal of a dish/stirling solar power plant in Greece based on an innovative solar concentrator formed by elastic film,” *Renewable Energy*, vol. 60, pp. 446–453, 2013, doi: 10.1016/j.renene.2013.05.031.

[23] A. M. A. Al-Dafaie, M. E. Dahdolan, and M. A. Al-Nimr, “Utilizing the heat rejected from a solar dish Stirling engine in potable water production,” *Solar Energy*, vol. 136, pp. 317–326, 2016, doi: 10.1016/j.solener.2016.07.007.

[24] L. S. Mendoza Castellanos, G. E. Carrillo Caballero, V. R. Melian Cobas, E. E. Silva Lora, and A. M. Martinez Reyes, “Mathematical modeling of the geometrical sizing and thermal performance of a Dish/Stirling system for power generation,” *Renewable Energy*, vol. 107, no. April, pp. 23–35, 2017, doi: 10.1016/j.renene.2017.01.020.

[25] K. Bataineh and Y. Taamneh, “Performance analysis of stand-alone solar dish Stirling system for electricity generation,” *International Journal of Heat and Technology*, vol. 35, no. 3, pp. 498–508, 2017, doi: 10.18280/ijht.350306.

[26] M. E. Zayed *et al.*, “Performance prediction and techno-economic analysis of solar dish/stirling system for electricity generation,” *Applied Thermal Engineering*, vol. 164, no. April 2019, p. 114427, 2020, doi: 10.1016/j.applthermaleng.2019.114427.

[27] A. Buscemi, V. lo Brano, C. Chiaruzzi, G. Ciulla, and C. Kalogeri, “A validated energy model of a solar dish-Stirling system considering the cleanliness of mirrors,” *Applied Energy*, vol. 260, no. December 2019, p. 114378, 2020, doi: 10.1016/j.apenergy.2019.114378.

[28] P. H. Shaikh, A. A. Lashari, Z. H. Leghari, and Z. A. Memon, “Techno- enviro-economic assessment of a stand- alone parabolic solar dish stirling system for electricity generation,” *International Journal of Energy Research*, no. January, pp. 1–21, 2021, doi: 10.1002/er.6513.

[29] S. Guo, Q. Liu, J. Sun, and H. Jin, “A review on the utilization of hybrid renewable energy,” *Renewable and Sustainable Energy Reviews*, vol. 91, no. April, pp. 1121–1147, 2018, doi: 10.1016/j.rser.2018.04.105.

[30] H. Wu, Q. Liu, Z. Bai, G. Xie, J. Zheng, and B. Su, “Thermodynamics analysis of a novel steam/air biomass gasification combined cooling, heating and power system with solar energy,” *Applied Thermal Engineering*, vol. 164, no. October 2019, p. 114494, 2020, doi: 10.1016/j.applthermaleng.2019.114494.

[31] L. Mastropasqua, I. Pecenati, A. Giostri, and S. Campanari, “Solar hydrogen production : Techno-economic analysis of a parabolic dish- supported high-temperature electrolysis system,” *Applied Energy*, vol. 261, no. September 2019, p. 114392, 2020, doi: 10.1016/j.apenergy.2019.114392.

[32] H. Shariatpanah, M. Z. Jahromi, and R. Fadaeinedjad, “Simulation of a new grid-connected hybrid generation system with Stirling engine and wind turbine,” *Journal of Renewable and Sustainable Energy*, vol. 5, no. 6, 2013, doi: 10.1063/1.4850475.

[33] A. Rahman, L. C. Saikia, and N. Sinha, “Automatic generation control of an interconnected two-area hybrid thermal system considering dish-stirling solar thermal and wind turbine system,” *Renewable Energy*, vol. 105, pp. 41–54, 2017, doi: 10.1016/j.renene.2016.12.048.

[34] Y. Kadri and H. Hadj Abdallah, “Performance evaluation of a stand-alone solar dish Stirling system for power generation suitable for off-grid rural electrification,” *Energy Conversion and Management*, vol. 129, pp. 140–156, 2016, doi: 10.1016/j.enconman.2016.10.024.

[35] E. S. Hrayshat and M. S. Al-Soud, “Solar energy in Jordan: Current state and prospects,” *Renewable and Sustainable Energy Reviews*, vol. 8, no. 2, pp. 193–200, 2004, doi: 10.1016/j.rser.2003.10.005.

[36] B. Hammad, A. Al-Sardeah, M. Al-Abed, S. Nijmeh, and A. Al-Ghandoor, “Performance and economic comparison of fixed and tracking photovoltaic systems in Jordan,” *Renewable and Sustainable Energy Reviews*, vol. 80, no. May, pp. 827–839, 2017, doi: 10.1016/j.rser.2017.05.241.

[37] H. Al-Hamidi and J. al Asfar, “Hybrid renewable energy system with minimum noise wind turbine,” *Renewable Energy*, vol. 114, pp. 581–587, 2017, doi: 10.1016/j.renene.2017.07.015.

[38] M. Ababneh, W. Kakish, O. A. Mohareb, and I. Etier, “Investigation of wind energy in jordan,” no. Iceges, pp. 15–17, 2009.

[39] Solargis, “Solar resource maps of Jordan.” https://solargis.com/maps-and-gis-data/download/jordan (accessed Jul. 03, 2020).
[40] “Department of Meteorology.” http://jmd.gov.jo/en
[41] M. Demand, R. Mdred, G. Subramani, V. K. Ramachandaramurthy, and P. Sanjeevikumar, “Techno-Economic Optimization of Grid-Connected Photovoltaic (PV) and Battery Systems Based on Maximum Demand Reduction (MDRed) Modelling in Malaysia”.
[42] M. A. S. Eldean, A. el Shahat, and A. M. Soliman, “A new modeling technique based on performance data for photovoltaic modules and horizontal axis wind turbines,” 2018, doi: 10.1177/0309524X17737052.
[43] K. Bourouni, T. B. M. Barek, and A. al Taee, “Design and optimization of desalination reverse osmosis plants driven by renewable energies using genetic algorithms,” *Renewable Energy*, vol. 36, no. 3, pp. 936–950, 2011, doi: 10.1016/j.renene.2010.08.039.
[44] P. Taylor, M. A. S. Eldean, and A. M. Soliman, “Desalination and Water Treatment A new visual library for modeling and simulation of renewable energy desalination systems (REDS),” no. April, pp. 37–41, 2013, doi: 10.1080/19443994.2013.777369.
[45] M. M. Hand, “Variable-Speed Wind Turbine Controller Systematic Design Methodology : A Comparison of Non-Linear and Linear Model- Based Designs Variable-Speed Wind Turbine Controller Systematic Design Methodology : A Comparison of Non-Linear and Linear Model- Based Des,” 1999.
[46] T. S. No, J. Kim, J. H. Moon, and S. J. Kim, “Modeling , control , and simulation of dual rotor wind turbine generator system,” *Renewable Energy*, vol. 34, no. 10, pp. 2124–2132, 2009, doi: 10.1016/j.renene.2009.01.019.
[47] G. Ahmad and U. Amin, “Design , construction and study of small scale vertical axis wind turbine based on a magnetically levitated axial fl ux permanent magnet generator,” *Renewable Energy*, vol. 101, pp. 286–292, 2017, doi: 10.1016/j.renene.2016.08.027.
[48] M. A. Sharaf Eldean, K. M. Rafi, and A. M. Soliman, “Performance analysis of different working gases for concentrated solar gas engines: Stirling & Brayton,” *Energy Conversion and Management*, vol. 150, no. August, pp. 651–668, 2017, doi: 10.1016/j.enconman.2017.08.008.
[49] S. C. K. and S. K. T. v. Siva Reddy, “Exergetic analysis and performance evaluation of parabolic dish Stirling engine solar power plant,” *Archives of Thermodynamics*, vol. 33, no. 4, pp. 23–40, 2012, doi: 10.1002/er.
[50] V. Thakkar, A. Doshi, and A. Rana, “Performance Analysis Methodology for Parabolic Dish Solar Concentrators for Process Heating Using Thermic Fluid Performance Analysis Methodology for Parabolic Dish Solar Concentrators for Process Heating Using Thermic Fluid,” no. October, 2019, doi: 10.9790/1684-1212101114.
[51] B. Kongtragool and S. Wongwises, “Optimum absorber temperature of a once-reflecting full conical concentrator of a low temperature differential Stirling engine,” vol. 30, pp. 1671–1687, 2005, doi: 10.1016/j.renene.2005.01.003.
[52] E. Gholamalizadeh and J. D. Chung, “Design of the Collector of a Solar Dish-Stirling System: A Case Study,” *IEEE Access*, vol. 5, pp. 20754–20762, 2017, doi: 10.1109/ACCESS.2017.2758354.
[53] B. Kongtragool and S. Wongwises, “A review of solar-powered Stirling engines and low temperature differential Stirling engines,” *Renewable and Sustainable Energy Reviews*, vol. 7, no. 2, pp. 131–154, 2003, doi: 10.1016/S1364-0321(02)00053-9.

[54] C. Cheng and H. Yang, “Theoretical model for predicting thermodynamic behavior of thermal-lag Stirling engine,” *Energy*, vol. 49, pp. 218–228, 2013, doi: 10.1016/j.energy.2012.10.031.

[55] A. Z. Hafez, A. Soliman, K. A. El-Metwally, and I. M. Ismail, “Solar parabolic dish Stirling engine system design, simulation, and thermal analysis,” *Energy Conversion and Management*, vol. 126, pp. 60–75, 2016, doi: 10.1016/j.enconman.2016.07.067.

[56] A. M. Soliman *et al.*, “A new system design of using solar dish-hydro combined with reverse osmosis for sewage water treatment: Case study Al-Marj, Libya,” *Desalination and Water Treatment*, vol. 193, no. July, pp. 189–211, 2020, doi: 10.5004/dwt.2020.25782.

[57] R. P. Shea and Y. Kumar, “Applied levelized cost of electricity for energy technologies in a small island developing state : A case study in Mauritius,” *Renewable Energy*, vol. 132, pp. 1415–1424, 2019, doi: 10.1016/j.renene.2018.09.021.

[58] M. Bruck, P. Sandborn, and N. Goudarzi, “A Levelized Cost of Energy (LCOE) model for wind farms that include Power Purchase Agreements (PPAs),” *Renewable Energy*, vol. 122, pp. 131–139, 2018, doi: 10.1016/j.renene.2017.12.100.

[59] “The Wind Power.” https://www.thewindpower.net/windfarms_list_en.php (accessed May 10, 2020).

[60] M. A. Al-Nimr and W. A. Al-Ammari, “A novel hybrid and interactive solar system consists of Stirling engine/vacuum evaporator/thermoelectric cooler for electricity generation and water distillation,” *Renewable Energy*, vol. 153, pp. 1053–1066, 2020, doi: 10.1016/j.renene.2020.02.072.

[61] A. J. Sultan, K. J. Hughes, D. B. Ingham, L. Ma, and M. Pourkashanian, “Techno-economic competitiveness of 50 MW concentrating solar power plants for electricity generation under Kuwait climatic conditions,” *Renewable and Sustainable Energy Reviews*, vol. 134, no. December 2019, p. 110342, 2020, doi: 10.1016/j.rser.2020.110342.

[62] K. Hirbodi, M. Enjavi-arsanjani, and M. Yaghoubi, “Techno-economic assessment and environmental impact of concentrating solar power plants in Iran,” *Renewable and Sustainable Energy Reviews*, vol. 120, no. December 2019, p. 109642, 2020, doi: 10.1016/j.rser.2019.109642.

[63] S. Mihoub, “Design , economic , and environmental assessments of linear Fresnel solar power plants,” no. November 2018, pp. 1–16, 2020, doi: 10.1002/ep.13350.

[64] S. Abdul-wahab, Y. Charabi, A. M. Al-mahruqi, and I. Osman, “Selection of the best solar photovoltaic (PV) for Oman,” *Solar Energy*, vol. 188, no. July, pp. 1156–1168, 2019, doi: 10.1016/j.solener.2019.07.018.

[65] M. Amin, V. Rad, A. Shahsavari, F. Rajaee, and A. Kasaeian, “Techno-economic assessment of a hybrid system for energy supply in the affected areas by natural disasters : A case study,” *Energy Conversion and Management*, vol. 221, no. March, p. 113170, 2020, doi: 10.1016/j.enconman.2020.113170.

[66] F. Al-turjman, Z. Qadir, M. Abujubbeh, and C. Batunlu, “Feasibility analysis of solar photovoltaic-wind hybrid energy system for household applications ☆,” vol. 86, 2020, doi: 10.1016/j.compeleceng.2020.106743.

[67] M. Chennaif, H. Zahboune, M. Elhafyani, and S. Zouggar, “Electric System Cascade Extended Analysis for optimal sizing of an autonomous hybrid CSP / PV / wind system with Battery Energy Storage System and thermal energy storage,” *Energy*, vol. 227, p. 120444, 2021, doi: 10.1016/j.energy.2021.120444.